Hansen, L., Conrad, C., Boneh, Y., Skemer, P., Warren, J., & Kohlstedt, D. (2016). Viscous anisotropy of textured olivine aggregates: 2. Micromechanical model. *Journal Of Geophysical Research: Solid Earth*, *121*(10), 7137-7160. http://dx.doi.org/10.1002/2016jb013240

DOI: 10.1002/2016jb013240

AGU PUBLICATIONS

JGR

Journal of Geophysical Research: Solid Earth

RESEARCH ARTICLE
10.1002/2016JB013240

Key Points:
- A micromechanical model is developed for estimating the viscous anisotropy of olivine aggregates
- A companion model is developed to predict the evolution of olivine crystal orientations at very large strains
- Both models are calibrated with recent experimental results, yielding new tools to be incorporated into large-scale geodynamics models

Supporting Information:
- Supporting Information S1
- Movie S1
- Movie S2

Correspondence to:
L. N. Hansen,
lars.hansen@earth.ox.ac.uk

Citation:
Hansen, L. N., C. P. Conrad, Y. Boneh, P. Skemer, J. M. Warren, and D. L. Kohlstedt (2016), Viscous anisotropy of textured olivine aggregates: 2. Micromechanical model, *J. Geophys. Res. Solid Earth*, *121*, 7137–7160, doi:10.1002/2016JB013240.

Received 7 JUN 2016
Accepted 25 SEP 2016
Accepted article online 27 SEP 2016
Published online 25 OCT 2016

Viscous anisotropy of textured olivine aggregates: 2. Micromechanical model

Lars N. Hansen[1], Clinton P. Conrad[2,3], Yuval Boneh[4], Philip Skemer[4], Jessica M. Warren[5], and David L. Kohlstedt[6]

[1]Department of Earth Sciences, University of Oxford, Oxford, UK, [2]Department of Geology and Geophysics, University of Hawai'i at Mānoa, Honolulu, Hawaii, USA, [3]Centre for Earth Evolution and Dynamics, University of Oslo, Oslo, Norway, [4]Department of Earth and Planetary Sciences, Washington University, St. Louis, Missouri, USA, [5]Department of Geological Sciences, University of Delaware, Newark, Delaware, USA, [6]Department of Earth Sciences, University of Minnesota, Twin Cities, Minneapolis, Minnesota, USA

Abstract The significant viscous anisotropy that results from crystallographic alignment (texture) of olivine grains in deformed upper mantle rocks strongly influences a large variety of geodynamic processes. Our ability to explore the effects of anisotropic viscosity in simulations of these processes requires a mechanical model that can predict the magnitude of anisotropy and its evolution. Unfortunately, existing models of olivine textural evolution and viscous anisotropy are calibrated for relatively small deformations and simple strain paths, making them less general than desired for many large-scale geodynamic scenarios. Here we develop a new set of micromechanical models to describe the mechanical behavior and textural evolution of olivine through a large range of strains and complex strain histories. For the mechanical behavior, we explore two extreme scenarios, one in which each grain experiences the same stress tensor (Sachs model) and one in which each grain undergoes a strain rate as close as possible to the macroscopic strain rate (pseudo-Taylor model). For the textural evolution, we develop a new model in which the director method is used to control the rate of grain rotation and the available slip systems in olivine are used to control the axis of rotation. Only recently has enough laboratory data on the deformation of olivine become available to calibrate these models. We use these new data to conduct inversions for the best parameters to characterize both the mechanical and textural evolution models. These inversions demonstrate that the calibrated pseudo-Taylor model best reproduces the mechanical observations. Additionally, the pseudo-Taylor textural evolution model can reasonably reproduce the observed texture strength, shape, and orientation after large and complex deformations. A quantitative comparison between our calibrated models and previously published models reveals that our new models excel in predicting the magnitude of viscous anisotropy and the details of the textural evolution. In addition, we demonstrate that the mechanical and textural evolution models can be coupled and used to reproduce mechanical evolution during large-strain torsion tests. This set of models therefore provides a new geodynamic tool for incorporating viscous anisotropy into large-scale numerical simulations.

1. Introduction

The viscosity of the upper mantle is a key parameter in many geodynamic processes. Although much work has been done developing constitutive models for upper mantle viscosity (for a review, see *Hirth and Kohlstedt* [2003]), the directional dependence of viscosity, that is, the anisotropy in viscosity, is still not well constrained. Several numerical investigations have demonstrated the potential for anisotropy in upper mantle viscosity to significantly modify geodynamic processes, with effects including modified styles of mantle convection [*Honda*, 1986; *Christensen*, 1987], enhanced magma production rates in subduction zones [*Lev and Hager*, 2011], increased spacing between gravitational instabilities beneath the lithosphere [*Lev and Hager*, 2008a], increased upper mantle temperatures [*Hearn et al.*, 1997], and modified postglacial rebound [*Christensen*, 1987; *Han and Wahr*, 1997]. Although some of the major geodynamic consequences of viscous anisotropy have been established, the parameterization of viscous anisotropy in these models is simplistic. The physical mechanism for generating the anisotropy is not explicitly specified, and therefore these models neglect the evolution of anisotropy, simplify the symmetry of anisotropy, and take the magnitude of anisotropy to be a free parameter.

Recent deformation experiments suggest that viscous anisotropy in upper mantle rocks can result from the formation of crystallographic alignment of olivine [*Hansen et al.*, 2012a, 2012b, 2016], which we refer to as

texture. Textural evolution in olivine is a protracted and complex process in which the rate of change in the orientation and strength of the texture depends on the kinematics, thermomechanical conditions, and presence of any preexisting texture (for a review, see *Skemer and Hansen* [2016]). If the details of textural evolution in olivine aggregates can be appropriately parameterized in a micromechanical model that explicitly relates crystallographic texture to bulk mechanical properties, then the details of the evolution of anisotropy in viscosity can be incorporated into large-scale geodynamic models. Furthermore, textural evolution in olivine relates directly to seismic anisotropy in the upper mantle, and a micromechanical model that predicts both textural evolution and viscous anisotropy can be used to link seismic observations to the magnitude of viscous anisotropy in Earth's interior.

Several such micromechanical models have previously been developed [e.g., *Ribe and Yu*, 1991; *Tommasi et al*., 2000], using as input the mechanical properties of olivine single crystals measured in laboratory experiments [e.g., *Durham and Goetze*, 1977; *Bai et al*., 1991] and implementing one of a variety of averaging schemes to predict bulk mechanical properties given a distribution of individual crystal orientations. These models also predict the evolution of that orientation distribution and the corresponding evolution in mechanical properties. Due to the mechanical complexity implicit in an aggregate of many interacting anisotropic crystals, precise formulations of the problem can be computationally intensive [*Lebensohn*, 2001; *Castelnau et al*., 2008]. More computationally efficient methods either consider individual grain interactions with a homogeneous effective medium [e.g., *Tommasi*, 1998; *Tommasi et al*., 1999, 2000] or neglect grain interactions altogether [*Ribe and Yu*, 1991; *Kaminski and Ribe*, 2001; *Kaminski et al*., 2004]. These formulations have been calibrated for simulation of olivine deformation through comparison to laboratory observations of olivine texture development [*Nicolas et al*., 1973; *Zhang and Karato*, 1995; *Boneh and Skemer*, 2014]. In some cases, these formulations reasonably reproduce mechanical behavior predicted by more computationally intensive methods [*Castelnau et al*., 2008]. Thus, these computationally efficient methods have been incorporated in multiscale models designed to predict the anisotropic behavior of geodynamic systems with complex deformation paths [*Castelnau et al*., 2009; *Tommasi et al*., 2009].

Some predictions of existing micromechanical models are at odds with aspects of the experimental results. Deformation experiments on single crystals of San Carlos olivine indicate that the viscosity can vary by over 2 orders of magnitude between crystals oriented to activate the weakest slip system and those oriented to activate the strongest slip system [*Bai et al*., 1991]. In addition, single crystals oriented such that essentially no shear stress is resolved on the available slip systems exhibit viscosities an order of magnitude larger than crystals oriented for slip on the hardest system [*Durham and Goetze*, 1977]. However, recent micromechanical models of polycrystalline olivine predict viscosities that vary with orientation of the applied stress by only a factor of ~3 [*Knoll et al*., 2009; *Tommasi et al*., 2009], suggesting that olivine aggregates exhibit relatively small viscous anisotropy. By contrast, recent laboratory experiments on strongly textured aggregates of olivine demonstrate that the magnitude of anisotropy can be at least an order of magnitude larger than that predicted by numerical simulations [*Hansen et al*., 2012a]. This discrepancy between model and experiment may occur in part because textures used in these models to predict mechanical properties are weaker, representing less preceding strain, than those present in the laboratory experiments. The mechanical predictions of the models tend to only be tested with relatively weak textures because of numerical instabilities that may arise with very strong textures [*Tommasi et al*., 2009]. Compounding these issues, model predictions of large deformations result in textures much stronger than those observed in laboratory experiments for the same total strain [*Tommasi*, 1998]. Thus, not only do the micromechanical models underpredict the magnitude of viscous anisotropy compared to laboratory experiments, but they are also limited in their applicability to large-scale geodynamic flows in which large deformations are common.

In Part 1, we presented results from a set of laboratory deformation experiments in which anisotropy in viscosity and textural development were explored for several deformation paths [*Hansen et al*., 2016]. Here we use the results from these experiments and those of *Hansen et al*. [2012a] to calibrate a new model of mechanical behavior and textural evolution in olivine aggregates optimized for large strain deformations. We initially treat these problems separately, first developing a micromechanical model to predict mechanical anisotropy for an aggregate with a given distribution of grain orientations and subsequently developing a model to predict the distribution of orientations for a given deformation path. Finally, we couple these two models to yield a method for simulating the evolution of anisotropy in the deforming upper mantle.

2. Methods

2.1. Micromechanical Model

2.1.1. Mechanical Anisotropy

Calculations of the mechanical anisotropy of plastically deforming polycrystalline materials often aim to describe aggregate behavior based on the physics of deforming single crystals. The complex mechanical problem of extrapolating single-crystal properties to an aggregate of a given distribution of grain orientations has received significant attention (for a recent review, see *Pokharel et al.* [2014]). Two end-member approaches are recognized. All individual grains can be either constrained to follow the macroscopic strain rate tensor [*Taylor*, 1938; *Bishop and Hill*, 1951] or constrained to all feel the macroscopic stress tensor [*Sachs*, 1928]. The former is often referred to as the Taylor or Taylor-Bishop-Hill model, which enforces strain compatibility but does not maintain stress equilibrium. The latter is often referred to as the Sachs or static model, which enforces stress equilibrium but does not maintain strain compatibility. Thus, both end-members make extreme assumptions about the nature of grain interactions. Although a variety of more sophisticated approaches for accounting for grain interactions exist [e.g., *Lebensohn and Tomé*, 1993; *Lebensohn*, 2001], we explore the applicability of these two end-members to our experimental data to make a first-order assessment of the role of texture in moderating mechanical behavior of an aggregate.

Crystallographic slip is characterized by the slip systems of active dislocations. Each slip system can be defined by a Burgers vector, **b**, and a normal to the slip plane, **n**. The dyadic $\mathbf{b} \otimes \mathbf{n}$ yields a symmetric tensor, M_{ij}, and a skew-symmetric tensor, Q_{ij}, given by

$$\begin{aligned} M_{ij}^{\alpha} &= \frac{1}{2}\left(b_i^{\alpha} n_j^{\alpha} + n_i^{\alpha} b_j^{\alpha}\right) \\ Q_{ij}^{\alpha} &= \frac{1}{2}\left(b_i^{\alpha} n_j^{\alpha} - n_i^{\alpha} b_j^{\alpha}\right), \end{aligned} \tag{1}$$

where the superscript α denotes the value for a particular slip system. Here we use the Einstein summation convention for subscripts. The symmetric tensor, **M**, is often referred to as the Schmid tensor and can be used to relate the applied deviatoric stress tensor, $\boldsymbol{\sigma}$, to the shear stress, τ, resolved on slip system α through the relation

$$\tau = M_{ij}^{\alpha} \sigma_{ij}. \tag{2}$$

The Schmid tensor can also be used to relate the resulting shear strain rate, $\dot{\gamma}$, due to slip on slip system α to the strain rate tensor, $\dot{\varepsilon}$, through the relation

$$\dot{\varepsilon}_{ij} = M_{ij}^{\alpha} \dot{\gamma}. \tag{3}$$

The above equations can be combined in a power law form and summed over all available slip systems, yielding [e.g., *Lebensohn and Tomé*, 1993]

$$\dot{\varepsilon}_{ij}^{g} = A \sum_{\alpha} M_{ij}^{\alpha} \left(\frac{M_{kl}^{\alpha} \sigma_{kl}}{\tau_{\mathrm{o}}^{\alpha}} \right)^{n}, \tag{4}$$

where A is a material constant (units of stress^n time^{-1}) and τ_{o} is a dimensionless scalar that describes the strength of the slip system. The value of τ_{o} in equation (4) is often referred to as the "critical-resolved shear stress," which, in the context of high-temperature creep, denotes the stress necessary to deform at a given strain rate. In addition, the reported values of τ_{o} are often normalized by the value for the weakest slip system. Here we instead define τ_{o} as the strength of the slip system relative to the isotropic strength of the aggregate. We also note that the aggregate can exhibit a sensitivity of the strain rate to the mean grain size if grain boundary processes are important in the deformation. Although equation (4) only describes the deformation of a single grain, as indicated by the superscripted g, the grain size sensitivity can still be included in this equation by substituting $A = B/d^p$, where B is a material constant (units of stress^n length^p time^{-1}), d is the mean grain size, and p is the grain size exponent. This approach assumes that the mechanical anisotropy results only from intragranular processes, and therefore the magnitude of anisotropy is not dependent on grain size. In our analysis below, the isotropic strength of the aggregate is that determined by *Hansen et al.* [2012b] for Fo_{50} olivine, for which equation (4) yields an isotropic response if all values of τ_{o} are equal to unity, $n = 4.1$, $p = 0.73$, and $B = 10^{-11.8}\ \mu m^{0.73}\ MPa^{-4.1}\ s^{-1}$.

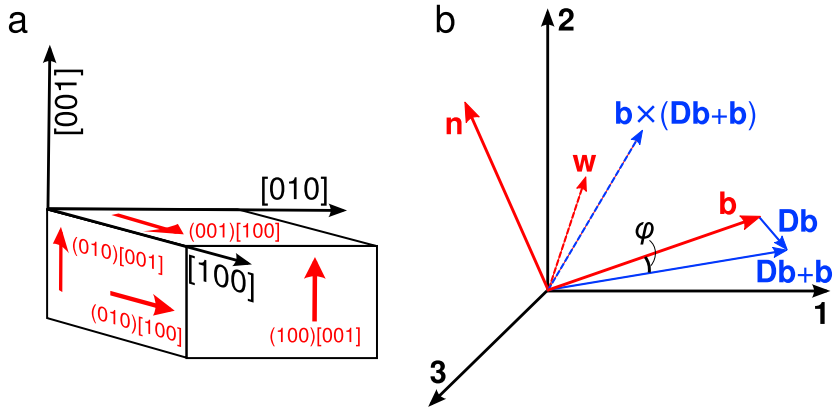

Figure 1. (a) Schematic diagram of the four olivine slip systems considered in this study in the crystallographic reference frame. (b) Schematic diagram illustrating the method for determining the rotation rate of a crystal due to the activity of a single slip system. The numbered black arrows depict the sample reference frame. The red arrows represent the coordinate system of the slip system defined by the Burgers vector, **b**, the normal to the slip plane, **n**, and the angular velocity, **w**, induced by activity of the slip system. The blue arrows indicate vectors involving the velocity gradient tensor, **D**, that are important in determining the rotation rate.

The Sachs model, on the one hand, assumes that every grain experiences the same stress tensor in the sample reference frame. Thus, if the orientation of each grain relative to the sample reference frame is taken into account when calculating M_{ij}, the strain tensors for all the grains can be calculated according to equation (4), and an arithmetic mean can be taken to describe the aggregate strain rate.

The Taylor model, on the other hand, requires the stress tensor to be determined numerically. The first step in this process is to determine the activities of each slip system from the aggregate strain rate tensor. This requires that the von Mises criterion be met, that is, that five linearly independent slip systems are available [*Mises*, 1928; *Groves and Kelly*, 1963]. For many materials, there are enough slip systems that the determination of the activities of the different slip systems is nonunique. Thus, *Bishop and Hill* [1951] assumed that the active slip systems are those that minimize the energy dissipation within the grain.

Unfortunately, the von Mises criterion is not met by olivine, for which the most often observed slip systems are (010)[100], (010)[001], (001)[100], and (100)[001], as drawn schematically in Figure 1a (for a summary of observations, see *Tommasi et al*. [2000]). Note that the latter two slip systems yield the same Schmid tensor since they are linearly dependent, and from here on, we will refer only to (001)[100]. Therefore, there are only three common, linearly independent slip systems in olivine. To meet the von Mises criterion, a common approach is to incorporate fictitious or rarely observed slip systems, using values of τ_o that are significantly larger than those for the common slip systems [e.g., *Tommasi et al*., 2000; *Castelnau et al*., 2008]. This ad hoc approach still allows the real slip systems to control the textural evolution, but the mechanical response is dominated by the fictitious slip systems [*Castelnau et al*., 2008]. Thus, introducing fictitious slip systems to satisfy the von Mises criterion is not desirable in the present study since our goal is to relate the experimentally measured anisotropy in viscosity to the available slip systems in olivine.

We instead use a simplified approach for the Taylor model by only considering the three common slip systems for olivine, which we refer to as the pseudo-Taylor model. For each grain, the strain rates on each slip system are determined by finding the closest approximation of the aggregate behavior using a least squares approach. Thus, we do not exactly replicate the aggregate strain rate tensor in each grain. A similar approach has been taken by previous authors [*Ribe and Yu*, 1991; *Kaminski and Ribe*, 2001; *Kaminski et al*., 2004], who suggest that the misfit between the calculated strain rate and the imposed strain rate would be accommodated by additional deformation processes such as grain boundary sliding and dislocation climb. In the case of olivine with only three slip systems, the best fit strain rate tensor is uniquely determined. Thus, an iterative minimization routine to find the set of slip systems with the least energy dissipation is not required, greatly reducing calculation time for the pseudo-Taylor model relative to the standard Taylor model.

2.1.2. Textural Evolution

We take a phenomenological approach to simulate rotations of individual grains within an aggregate. To do this, we account for rotations associated with slip on individual slip systems and induced by deformation represented by the macroscopic velocity gradient tensor, **D**. The orientation of the Burgers vector and the normal to the slip plane in the sample reference frame can be found through

$$\begin{aligned}\mathbf{n}^{\alpha,s} &= \mathbf{q}\mathbf{n}^{\alpha}\mathbf{q}^{-1}\\ \mathbf{b}^{\alpha,s} &= \mathbf{q}\mathbf{b}^{\alpha}\mathbf{q}^{-1},\end{aligned} \tag{5}$$

where **q** is a quaternion describing the grain orientation and the superscript s denotes the sample reference frame. We estimate the angular velocity due to slip on a slip system using an approach inspired by the director method [*Mühlhaus et al*., 2002, 2004]. In the director method, the rate of change in orientation of a line, the director, is given by the product of the velocity gradient tensor, **D**, and the director. Thus, the director gradually becomes aligned with the dominant flow direction (in 2-D) or dominant shear plane (in 3-D). The director method has been used for simulating textural evolution and exhibits the benefit of being relatively stable for large deformations [*Lev and Hager*, 2008a]. However, as we still intend for the slip systems to control grain rotations, we suggest that the *rate* of rotation due to slip on a slip system can be approximated by the matrix product **Db** such that the Burgers vector acts as the director. More specifically, as depicted in Figure 1b, we assume that the angular velocity scales with φ, the angle between **b** and **Db** + **b**. The angular velocity due to slip on slip system α can then be defined as

$$\mathbf{w}^{\alpha} = a^{\alpha} f^{\alpha} \varphi^{\alpha} \|\mathbf{n}^{\alpha,s} \times \mathbf{b}^{\alpha,s}\|, \tag{6}$$

where the cross product of **n** and **b** yields the orientation of the angular velocity vector. The magnitude of the angular velocity is given by the product $af\varphi$, where f is a constant that determines the relative rotation rate for each slip system and a is the sign of the angular velocity. The value of a is given by

$$a^{\alpha} = \mathrm{sgn}\left\{(\mathbf{b}^{\alpha} \times [\mathbf{D}\mathbf{b}^{\alpha} + \mathbf{b}^{\alpha}]) \cdot \mathbf{w}^{\alpha}\right\}, \tag{7}$$

which yields +1 if the rotation vector associated with the director method, $\mathbf{b} \times [\mathbf{Db} + \mathbf{b}]$, is within 90° of **w** and yields −1 if it is more than 90° from **w**. The result of this approach is that the orientation of **b** relative to the flow determines the *driving force* for rotation, but the *axis of rotation* is constrained to be parallel to $\mathbf{n} \times \mathbf{b}$.

The total angular velocity of a grain due to slip on all of that grain's available slip systems is given by

$$\mathbf{w} = \sum_{\alpha} \mathbf{w}^{\alpha}. \tag{8}$$

The rate of change of the grain orientation can then be defined as

$$\dot{\mathbf{q}} = \frac{1}{2}\mathbf{w}\mathbf{q}. \tag{9}$$

This differential equation therefore relates the rate of change in orientation to the macroscopic flow, **D**, the available slip systems and their relative activities, f^{α}, and the current orientation of the grain, **q**.

For olivine, we suggest that experimentally determined textures can be sufficiently replicated using the commonly observed slip systems. Although (100)[001] and (001)[100] are linearly dependent in our mechanical model, reducing the number of independent slip systems to three, their different Burgers vectors will lead to different values of φ and therefore different angular velocities. That is, these two slip systems contribute similarly to mechanical behavior but differently to grain rotations. Thus, we consider four different slip systems in the textural evolution model, leading to four free parameters: $f^{(010)[100]}$, $f^{(001)[100]}$, $f^{(100)[001]}$, and $f^{(010)[001]}$. The relative values of these four parameters determine the relative contribution of each slip system to the textural evolution. In addition, the overall rate of textural evolution can be increased or decreased by equally increasing or decreasing all four values of f. Equation (9) can be solved numerically to find the grain orientation at any time during the deformation. We solve this equation using a low-order pair of Runge-Kutta formulas implemented in the MATLAB® function "ode23" [*Bogacki and Shampine*, 1989], which adaptively selects the size of each time step. For simplicity, we treat grains individually with no grain interaction, allowing calculations of the evolution of each grain orientation to occur in parallel.

Processes other than dislocation glide can modify textural evolution. Experimental observations suggest that dynamic recrystallization [*Karato*, 1988; *Lee et al*., 2002] and sliding along grain boundaries [e.g., *Rutter et al*., 1994] have an influence on grain orientations. Some of these phenomena have been incorporated into

textural evolution models [e.g., *Zhang et al*., 1994; *Lebensohn et al*., 1998; *Kaminski and Ribe*, 2001; *Blackman et al*., 2002; *Kaminski et al*., 2004], but the best method of parameterization largely remains unclear. We therefore take a simplified, empirical approach by assuming that these secondary processes can be accounted for by adjusting the values of f^α to best fit the observed textures. Our estimate of the rotation rate (equation (6)) is fundamentally based on the director method [*Mühlhaus et al*., 2002, 2004], for which $f = 1$ describes the kinematics of a marker line passively rotating in shear flow. In our application to olivine grain rotations, values of $f^\alpha < 1$ imply that slip on that slip system is impeded enough to result in rotations that are slower than a passive marker, while values of $f^\alpha > 1$ imply that slip on that slip system is enhanced in a manner that enhances rotation rates relative to a passive marker.

2.2. Experimental Data Sets for Comparison

Measured stresses and strain rates are taken from the experiments reported by *Hansen et al*. [2012a, 2016], which were conducted on aggregates of Fe-rich olivine (Fo_{50}) at a temperature of 1200°C, confining pressure of 300 MPa, equivalent stresses of 60–290 MPa, and equivalent strain rates of $0.1–5.9 \times 10^{-4}\,s^{-1}$. These studies deformed olivine aggregates sequentially under different loading geometries. In the first [*Hansen et al*., 2012a], samples were initially deformed in torsion to establish a clear crystallographic texture and subsequently deformed in extension. In the second [*Hansen et al*., 2016], samples were initially deformed in extension and subsequently deformed in torsion. In both cases, the initial deformation established a texture that caused a decrease in viscosity by the end of the experiment. However, the established texture led to an increase in viscosity in the subsequent test with a different loading geometry. The minimum viscosity was consistently less than the maximum viscosity by a factor of >10.

In addition to mechanical data, measured textures are also taken from the experiments reported in the two studies discussed above [*Hansen et al*., 2012a, 2016]. We also include textures presented by *Hansen et al*. [2014] from samples deformed in torsion without any prior or subsequent extensional deformation. Figure 2 presents representative examples of the three primary textures in this data set. Samples were initially formed by hot pressing olivine powders, directly after which crystal orientations were uniformly distributed (Figure 2, bottom row). Torsional deformation established a texture in which [100] axes align with the shear direction and [010] and [001] axes were girdled at low strain and aligned with the normal to the shear plane and parallel to the vorticity direction, respectively, at high strain (Figure 2, top row). In contrast, extensional deformation established small-circle girdles of [100] and [001] axes close to the extension direction and girdles of [010] axes normal to the extension direction (Figure 2, middle row). In addition, samples initially deformed in extension and subsequently deformed in torsion revealed a protracted textural evolution that eventually resulted in textures at high strain similar to those formed by torsion of hot-pressed samples.

2.3. Model Inversion

Our mechanical model for relating applied stress, resulting strain rate, and the distribution of grain orientations relies on only three parameters (τ_o for each of the three independent slip systems), which allows for relatively straightforward determination of the best fit set of parameters. We define the misfit between the model and observations as the sum of squared errors between measured stresses or strain rates and the stresses or strain rates predicted by the pseudo-Taylor or Sachs models, respectively. To simulate mechanical behavior, we use the measured texture best representing the microstructural state at the time of the mechanical test. Specifically, mechanical data from the peak stress of experiments are modeled using the uniform texture induced by hot pressing (Figure 2, bottom row), and data points from high-strain portions of the experiments are modeled using the texture measured at the end of the experiment. For torsion tests, we assume that there are no axial deviatoric stresses (i.e., only σ_{12} and σ_{21} are nonzero) in calculations with the Sachs model and no axial strains (i.e., only $\dot{\varepsilon}_{12}$ and $\dot{\varepsilon}_{21}$ are nonzero) in calculations with the pseudo-Taylor model.

The textural evolution model described above also relies on few enough parameters that best fit values for the four values of f^α can be determined quantitatively. For each experiment, we use the measured initial texture as the starting texture for the model calculation and impose the same deformation as imposed in the experiment, again assuming that no axial strain occurred. The modeled texture is then compared to the texture measured from the experimentally deformed samples. The experimental data set [*Hansen et al*., 2012a, 2014, 2016] covers a wide range of finite strain, with samples deformed to a maximum shear strain of 18.2. However, the majority of the data come from samples deformed to relatively small strains, with 33

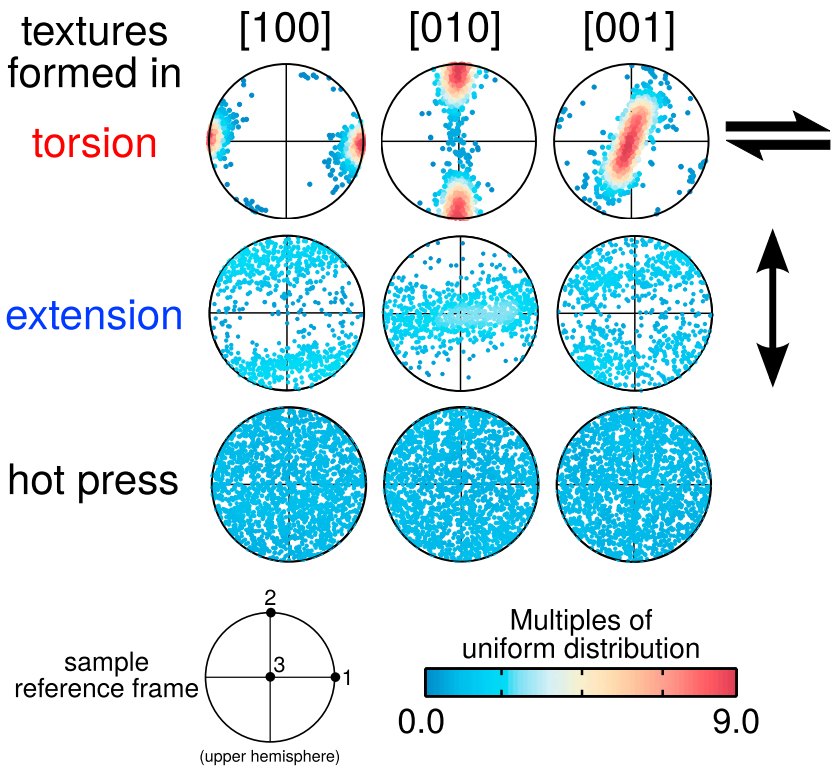

Figure 2. Representative textures from the data sets of *Hansen et al.* [2014, 2016] for samples formed by hot pressing and samples deformed in torsion and extension. Pole figures are plotted in the lower hemisphere and as one point per grain with the color of the data point corresponding to the value of the orientation distribution function. All pole figures are on the same color scale. Black arrows indicate the dominant deformation direction in deformed samples. A key to the reference frame is presented with numbers corresponding to the indices used when referring to elements of the stress and strain rate tensors.

out of 56 textures coming from samples deformed to shear strains $\leq$3. Thus, our data set is particularly sensitive to the portion of the strain history during which there is the greatest degree of textural evolution.

We compare modeled textures to textures measured in deformed samples using their calculated orientation distribution functions (ODFs). Each ODF is discretized over all possible representations of ODFs through linear combinations of radially symmetric functions, as implemented in MTEX and described by *Hielscher and Schaeben* [2008]. The values of the discretized ODFs for the modeled and measured textures are normalized with respect to the measured texture and compared with each other. The misfit is defined as the sum of the squared errors between the two ODFs. This procedure is encapsulated in the "calcError" function in MTEX [*Bachmann et al.*, 2010]. The misfits for all textures are summed to define a total misfit for the data set.

For both models, we sought to find the minimum misfit using a genetic algorithm, which is a directed random search method that utilizes the principles of natural selection and evolution to solve complex inverse problems [e.g., *Goldberg*, 1989; *Forrest*, 1993] and has been employed previously in the earth sciences [e.g., *King*, 1995; *Conrad et al.*, 2004]. This method is especially useful for problems that are not easily linearized and for which the possible solution space is too large to explore using randomized or grid search methods. To obtain optimal solutions, we maintain a population of 80 possible solutions to the forward problem, which are expressed as values of τ^{α} or f^{α} (for the micromechanical and textural models, respectively) for each slip system, expressed in binary form and concatenated into a single sequence. We randomly select initial values for these solutions by picking random values for the binary units ("bits") that express the exponent of each value of τ^{α} or f^{α} (chosen so that $10^{-4} < \tau^{\alpha} < 10^{2}$ and $0 < f^{\alpha} < 10$). The frequency with which each "individual" solution is propagated into subsequent "generations" is based on that individual's "fitness," which is its ability to minimize the defined misfit parameter. Here we select individuals for the next generation with a relative frequency proportional to the inverse square of their misfit. Solution diversity is added to each generation

by allowing 60% of solution pairs to undergo "crossover," in which the fraction of the solution ahead of a randomly selected location on the binary string is switched with that of another individual. Additionally, individual bits in each solution are switched, or "mutated," 2% of the time. Finally, we retain the single best fitting solution between generations to maintain continuity. The eventual best fitting solution is typically achieved after only 50 or fewer generations, but we run our genetic algorithm for 100 generations for completeness.

We also quantify the ability of our data set to constrain the model parameters for mechanical anisotropy and textural evolution. For each of the two models, we performed a grid search of model parameters in the neighborhood of the values determined with the genetic algorithm optimization.

2.4. Textural Characterization

Crystallographic textures in both experiments and simulations are characterized in terms of their strength, orientation, and symmetry. To evaluate the strength of a texture, we utilize both the M-index [*Skemer et al*., 2005] and the J-index (also known as the texture index) [*Bunge*, 2013, pp. 88–89]. The M-index is based on the distribution of uncorrelated misorientation axes and scales from 0 (uniform texture) to 1 (single-crystal texture). The J-index is based on the sharpness of the orientation distribution function and scales from 1 (uniform texture) to infinity (single-crystal texture). We calculate orientation distribution functions with the MTEX toolbox for MATLAB® [*Bachmann et al*., 2010] using a kernel halfwidth of 10°.

The orientation of the texture can be described with the corresponding eigenvectors, λ_1, λ_2, and λ_3. Many previous authors have described the orientation of the texture using the angle between the average or median [100] direction and the shear plane or shear direction [*Zhang and Karato*, 1995; *Tommasi et al*., 2000; *Zhang et al*., 2000; *Kaminski and Ribe*, 2001; *Warren et al*., 2008; *Skemer et al*., 2012]. We produce a similar measurement using the angle between λ_1 for [100] axes and the shear direction [*Hansen et al*., 2014; *Hansen and Warren*, 2015]. We additionally characterize the orientation of the distributions of [010] and [001] axes. Because these latter axis distributions tend to be girdled [*Hansen et al*., 2014, 2016], we describe them using the vector normal to the best fit girdle, that is, the angle between λ_3 and the shear direction.

To evaluate the symmetry of a texture, we use the eigenanalysis presented by *Vollmer* [1990]. We utilize the shape parameters, *P*, *G*, and *R*, which are defined from the eigenvalues of the orientation tensor describing the distribution of one particular crystallographic axis. An axis distribution that clusters into a point maximum has a value of *P* that approaches unity. A distribution that lies in a single plane forming a girdle has a value of *G* that approaches unity. A distribution that is uniformly distributed has a value of $R = 1$. These parameters are defined such that $P + G + R = 1$, which allows them to be displayed on a ternary diagram.

2.5. Implementation of Previously Published Models

We additionally compare our micromechanical model to two widely used models, VPSC [e.g., *Lebensohn and Tomé*, 1993; *Tommasi et al*., 2000] and D-Rex [*Kaminski and Ribe*, 2001; *Kaminski et al*., 2004]. For both previously published models, we use parameters recently determined to fit best the textural evolution observed in deformation experiments on Åheim dunite, a coarse-grained natural rock with a strong preexisting texture [*Boneh et al*., 2015]. For VPSC, a single nondimensional parameter (termed β here to avoid confusion with other parameters but termed α in *Tommasi et al*. [2000] and *Boneh et al*. [2015]) is used to simulate grain interactions ranging from $\beta = 0$, which corresponds to the Taylor model, and $\beta =$ infinity, which corresponds to the Sachs model. The range of β often used is between 1 and 100, which reproduces a wide range of experimental observations [*Tommasi et al*., 2000]. For the present study, we use $\beta = 100$ for the simulation used for texture analysis, following the results of *Boneh et al*. [2015] and $\beta = 1$ for simulations used for the mechanical analysis, to maintain consistency with studies by *Tommasi et al*. [2000, 2009].

For D-Rex, two nondimensional parameters, M^* and λ^*, are used to simulate dynamic recrystallization via grain boundary migration and nucleation of strain-free grains, respectively. Both parameters influence textural evolution, but M^* is most dominant in determining the overall influence of dynamic recrystallization on texture [e.g., *Hedjazian and Kaminski*, 2014]. Many prior studies have used $M^* = 125$, the value suggested by *Kaminski and Ribe* [2001] based on comparisons to the experimental results of *Zhang and Karato* [1995]. However, if preexisting textures are present, any subsequent textural evolution is slower, and a lower value for M^* is more consistent with experimental observations [*Boneh et al*., 2015]. Another parameter, χ, simulates the effects of grain boundary sliding on texture development by defining a grain size threshold below which no grain rotation occurs [*Kaminski et al*., 2004]. In the present study, we use values of $M^* = 10$, $\lambda^* = 5$, and

Table 1. Best Fit Model Parameters

	Mechanical Models		Texture Evolution Model
Slip System	Sachs Model, τ_0	Pseudo-Taylor Model, τ_0	f
(010)[100]	1.44	0.30	1.35
(001)[100]	0.57	0.27	1.45
(010)[001]	0.95	1.29	0.07
(100)[001]	—	—	0.14

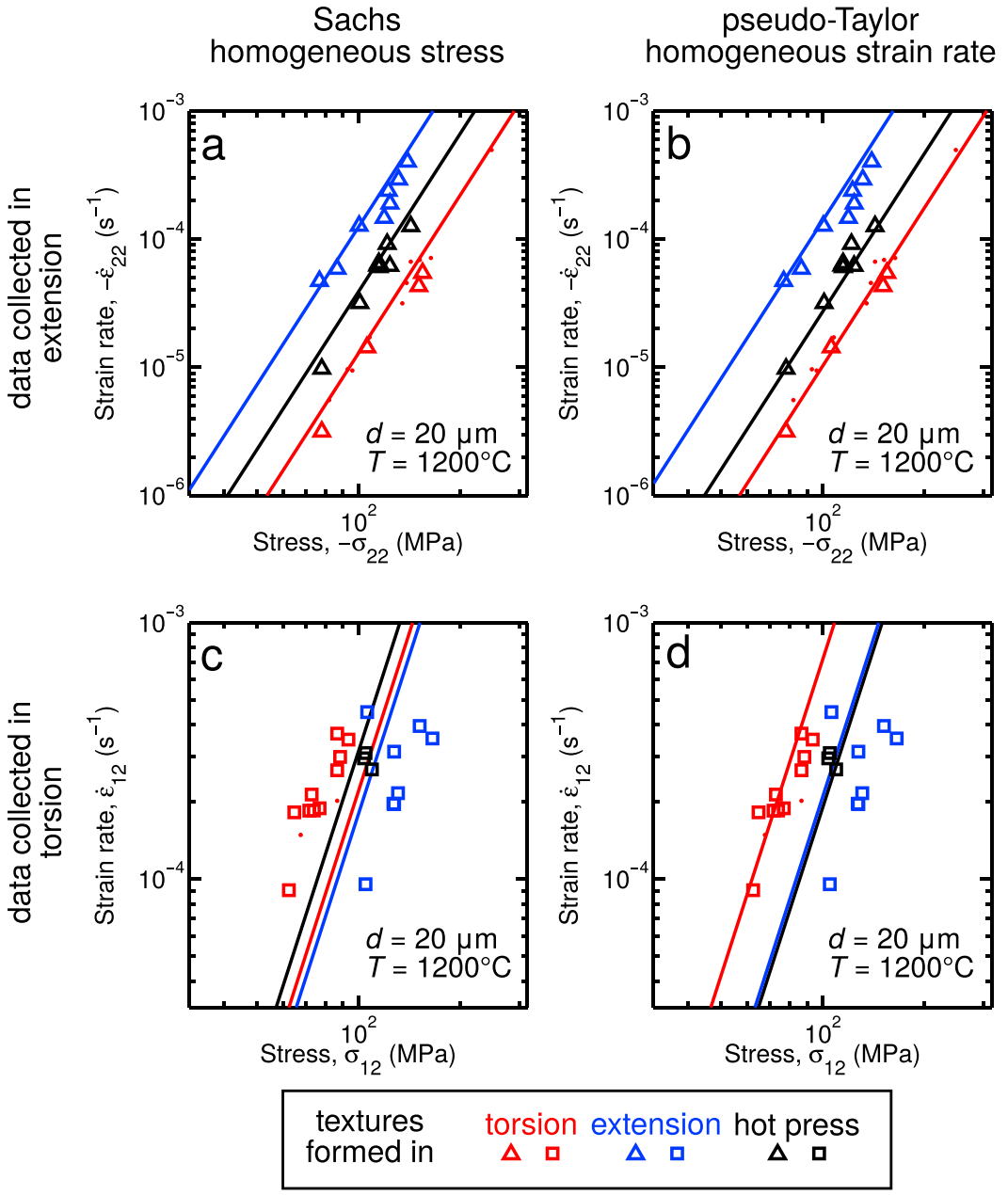

Figure 3. Mechanical data compared to predictions from the mechanical model. Individual data points come from *Hansen et al.* [2012a, 2016]. Solid lines are the results of model inversions. (a and b) Results from mechanical data collected in extension experiments. (c and d) Results from mechanical data collected in torsion experiments. Red dots are data from *Hansen et al.* [2012a]. Colors indicate the method by which samples were deformed prior to collection of the data presented in the figure. The results for model inversions are presented for (Figures 3a and 3c) the Sachs model and (Figures 3b and 3d) the pseudo-Taylor model.

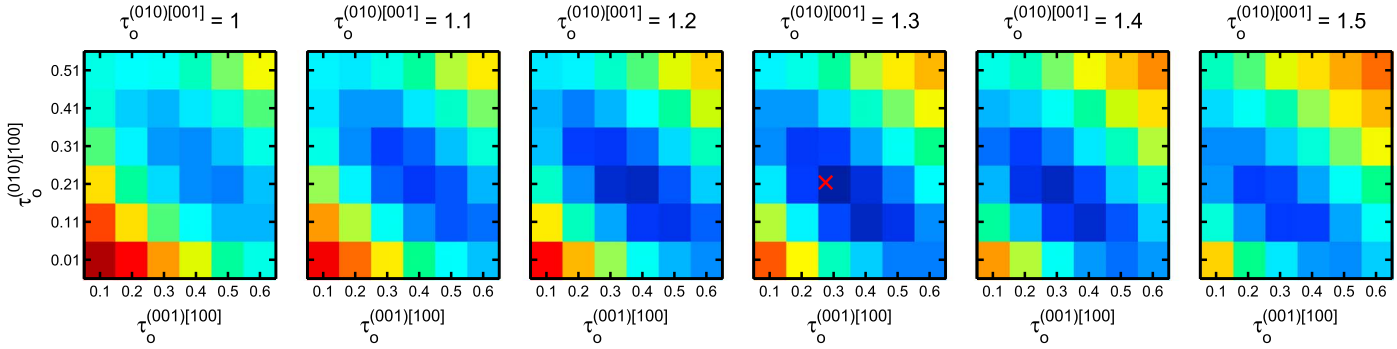

Figure 4. Sensitivity testing of the mechanical model to variations in the relative strengths of the three active slip systems, τ_o^{α}. Results are presented for the pseudo-Taylor model. The color scale indicates the total misfit between predicted strain rates and observed strain rates, as described in section 3.1. Colder colors indicate lower misfit. The red cross indicates the best fit set of parameters determined with the genetic algorithm.

$\chi = 0.3$ for grain boundary mobility, grain nucleation, and grain boundary sliding, respectively. Simulations with VPSC and D-Rex are not carried out to shear strains greater than 10 because these models are known to exhibit stability issues at high strains. These strains are still large enough to generate some initial instabilities with VPSC and D-Rex, but we include them to assess the magnitude of those fluctuations in comparison to fluctuations in our model.

3. Results

3.1. Mechanical Anisotropy Model

The best fit values of τ_o are presented in Table 1 for both the Sachs and pseudo-Taylor models. Each of these models is compared to the mechanical data for extension and torsion tests in Figure 3. The comparison is made by selecting a representative texture from our data set for each of the three main texture types (uniform after hot pressing powders, formed in extension, and formed in torsion) and calculating the stress tensor for several different values of the strain rate tensor (lines in Figure 3).

Both models agree well with the mechanical response measured in extension (Figures 3a and 3b). The predicted mechanical response associated with a uniform texture formed during the initial hot pressing (black symbols) agrees with data from samples deformed to very low strain such that they are effectively isotropic. The predicted mechanical response and measured data for samples with a texture formed in torsion (red symbols) are stronger than the isotropic case during extension. The predicted mechanical response and measured data for samples with a texture formed in extension (blue symbols) are weaker than the isotropic case.

However, both models struggle to predict the mechanical response measured in torsion (Figure 3c and 3d). The best fit values for the Sachs model dramatically underpredict the magnitude of anisotropy for deformation in torsion (Figure 3c). In addition, a key shortcoming of the Sachs model is that the relative magnitudes of stresses and strain rates for samples with different textures are incorrectly predicted for torsion tests (that is, the order of the red, black, and blue curves does not match the order of the red, black, and blue data). This phenomenon was ubiquitous throughout our testing of different parameter values for the Sachs model. In contrast, the best fit values for the pseudo-Taylor model match the observations well for most of the experiments conducted in torsion (Figure 3d). Yet, the pseudo-Taylor model does not predict a stronger-than-isotropic mechanical response for samples with a texture formed in extension (blue symbols), which is one of the major shortcomings of the model. However, as described below, the data sets for hot-pressed samples deformed in torsion and those for samples initially deformed in extension and subsequently deformed in torsion are within error of each other. Because the pseudo-Taylor model reasonably predicts the majority of the data set and correctly predicts the relative strengths of samples with different textures, we suggest that it is more applicable to our data set than the Sachs model.

The sensitivity of the pseudo-Taylor model to different parameter values is illustrated by the grid search presented in Figure 4. The misfit between model and data is presented as a function of three different variables. Each subplot examines the misfit for combinations of $\tau_o^{(010)[100]}$ and $\tau_o^{(001)[100]}$ while keeping $\tau_o^{(010)[001]}$ constant.

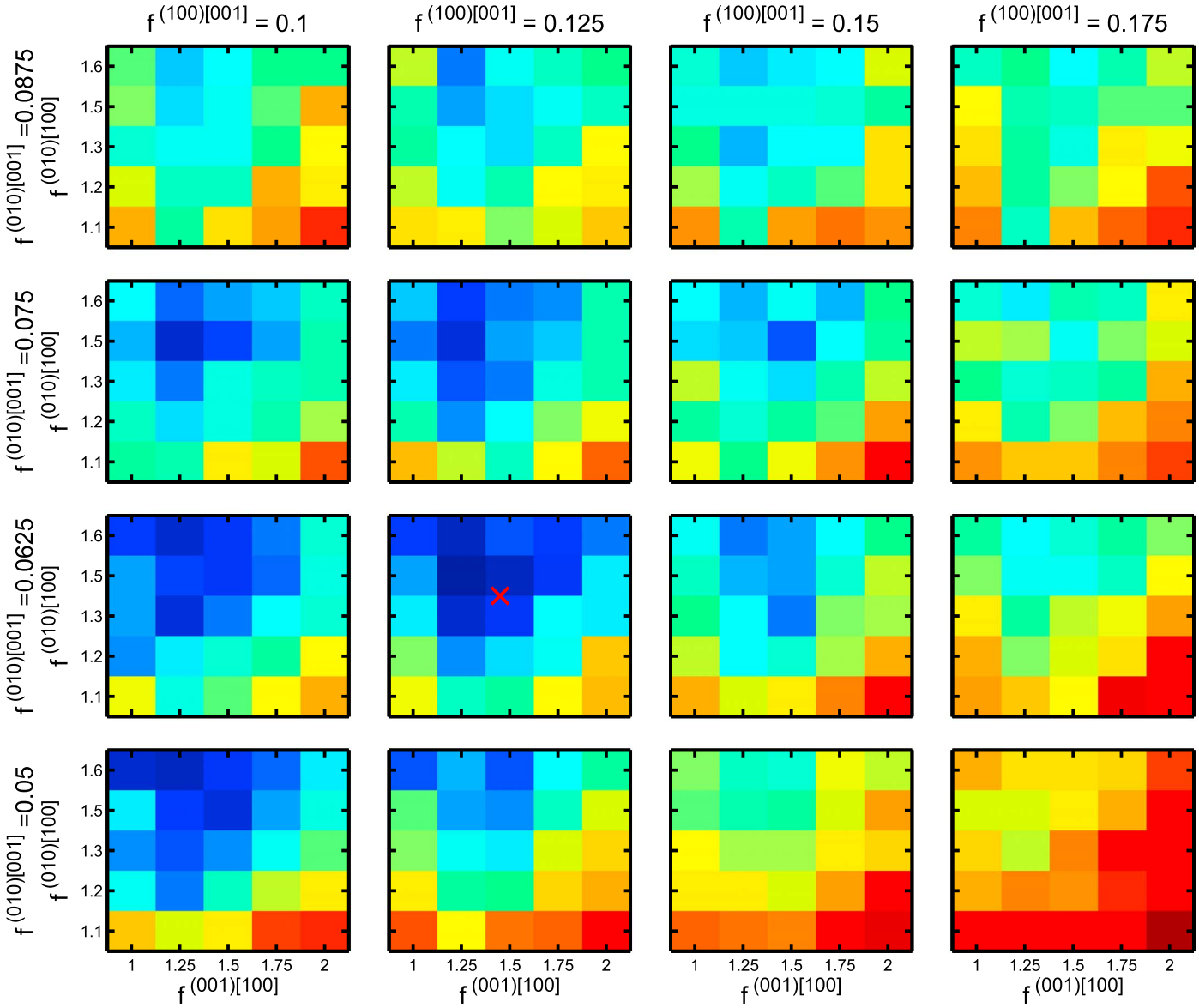

Figure 5. Sensitivity testing of the textural evolution model to variations in the relative rotation rates of the four active slip systems, f^{α}. The color scale indicates the total misfit between predicted textures and observed textures, as described in section 3.2. Colder colors indicate lower misfit. The red cross indicates the set of best fit parameters determined with the genetic algorithm.

Although there appears to be some covariance among parameters, it is clear that our data set is sensitive to each of the three parameters with a well-defined minimum. This minimum is also in reasonable agreement with the best fit determined by the genetic algorithm minimization (red cross).

3.2. Textural Evolution Model

3.2.1. Best Fit Model Parameters

The best fit values of f^{α} determined with the genetic algorithm are presented in Table 1. Results of our subsequent grid search are presented in Figure 5 as a grid of plots with misfit values in four-dimensional parameter space. Gradients in misfit are apparent in each dimension, indicating that the definition of misfit employed is sensitive to all of the free parameters. Values of misfit are particularly sensitive to changes in the value of $f^{(100)[001]}$, even though the best fit value for this parameter is significantly lower than the other values of f^{α}. Thus, our results suggest that rotation due to slip on (100)[001] only plays a small role in olivine textural evolution but is still critical to reproducing the laboratory observations.

The best fit values of f^{α} have relative magnitudes similar to the inverse of the best fit values of τ_0 determined for the pseudo-Taylor model. Normalized by $f^{(010)[100]}$, the best fit values of f^{α} for (010)[100], (001)[100], and (010)[001] are 1.00, 1.07, and 0.05, respectively. The corresponding normalized values of $1/\tau^{\alpha}$ are 1.00, 1.11, and 0.24. Interestingly, the slip system (010)[100] consistently appears stronger and contributes less to grain rotation than (001)[100], even though (010)[100] in olivine is often taken to (1) be the weakest slip system and (2) control the textural evolution. Although care should be taken to not overinterpret the results of our empirical model, this last observation does imply that the relationship between textural evolution and the relative strength of available slip systems is not as simple as often assumed.

3.2.2. Predicted Textural Evolution

In general, the predicted textural evolution is consistent with textures observed in the experiments. To demonstrate the fidelity of the model, we first select the most complicated deformation path for detailed comparison in Figure 6. This deformation path consists of initial extension followed by torsion, in which the textural evolution during the torsion experiment is influenced by the preexisting texture formed in extension [*Hansen et al*., 2016]. This comparison is also presented as an animation in the online supporting information (Movie S1). We use 200 grain orientations from the texture measured in the lowest-strain portion of sample PT0718 for a starting texture in the simulation and carry out the calculation to a shear strain of 10.1. Inclusion of fewer grains leads to poor representation of the texture characteristics [*Ismaïl and Mainprice*, 1998; *Skemer et al*., 2005], while inclusion of more grains leads to increased computational costs since the computation time scales approximately linearly with the number of grains.

There are several key similarities between the experimental observations and the numerical simulations of samples deformed in torsion after being deformed in tension. Most notably, the strain necessary to reorient the average [100] and [010] axes is similar between both data sets, reaching an approximately stable pattern by a shear strain of ~3. Girdles of [010] axes are present in both data sets at low strain and transform into point maxima at higher strain, similar to observations reported by *Hansen et al*. [2014]. Girdles of [001] axes are also present in both data sets, and, interestingly, both experiment and model exhibit girdles that are subtly inclined toward the shear direction.

Some differences also exist between the experimental observations and the numerical simulations of samples deformed in torsion after being deformed in tension. At shear strains less than 1.7, the experimental data set exhibits a broader distribution of [100] axes than the simulations, and the change in average [100] direction primarily occurs through the decay of one maximum in the [100] axis distribution at high angle to the shear direction and the growth of another maximum more closely aligned with the shear direction. We previously suggested that this feature may be related to recrystallization phenomena such as the nucleation of new grains in soft orientations [*Hansen et al*., 2016]. Although the calibration presented here is designed to be versatile enough to replicate textural development in samples in which dynamic recrystallization is occurring throughout deformation, it is constrained to the same population of grains throughout. Thus, our model cannot replicate scenarios in which certain grain orientations are favorably created or destroyed as a result of recrystallization. In addition, at high strain, some weak girdling is apparent in the [100] distribution of the simulated data set, whereas the [100] axes are distinctly point maxima in the experimental data set.

We assess the similarities among all experimental and simulated textures through a variety of metrics in Figures 7–9. Simulated textures for several deformation histories are compared to data from deformation experiments [*Hansen et al*., 2014, 2016] and data from a suite of naturally deformed dunites [*Warren et al*., 2008; *Hansen and Warren*, 2015]. Individual orientation distributions are characterized in terms of their strength, symmetry, and orientation [e.g., *Boneh and Skemer*, 2014].

Our simulations of extension experiments agree reasonably well with observations in terms of the strength (Figure 7) and symmetry (Figure 9) of the texture. The key discrepancy is in the orientation of the [001] distributions (Figure 8). In the simulations, [001] axes are distributed in a girdle normal to the extension axis, whereas in the experiments, the dominant direction is at an angle of ~45° to the tension axis. The apparent misalignment in the experiments is likely a result of the development of small-circle girdles in the [001] distributions, a phenomenon that is not reproduced in the simulations.

Simulations of textural evolution during torsion of samples with no initial texture and torsion of samples with an initial texture formed in extension also exhibit good agreement with experimental data. The simulations do particularly well in reproducing the rate of increase in the texture strength (Figure 7) and the rate of

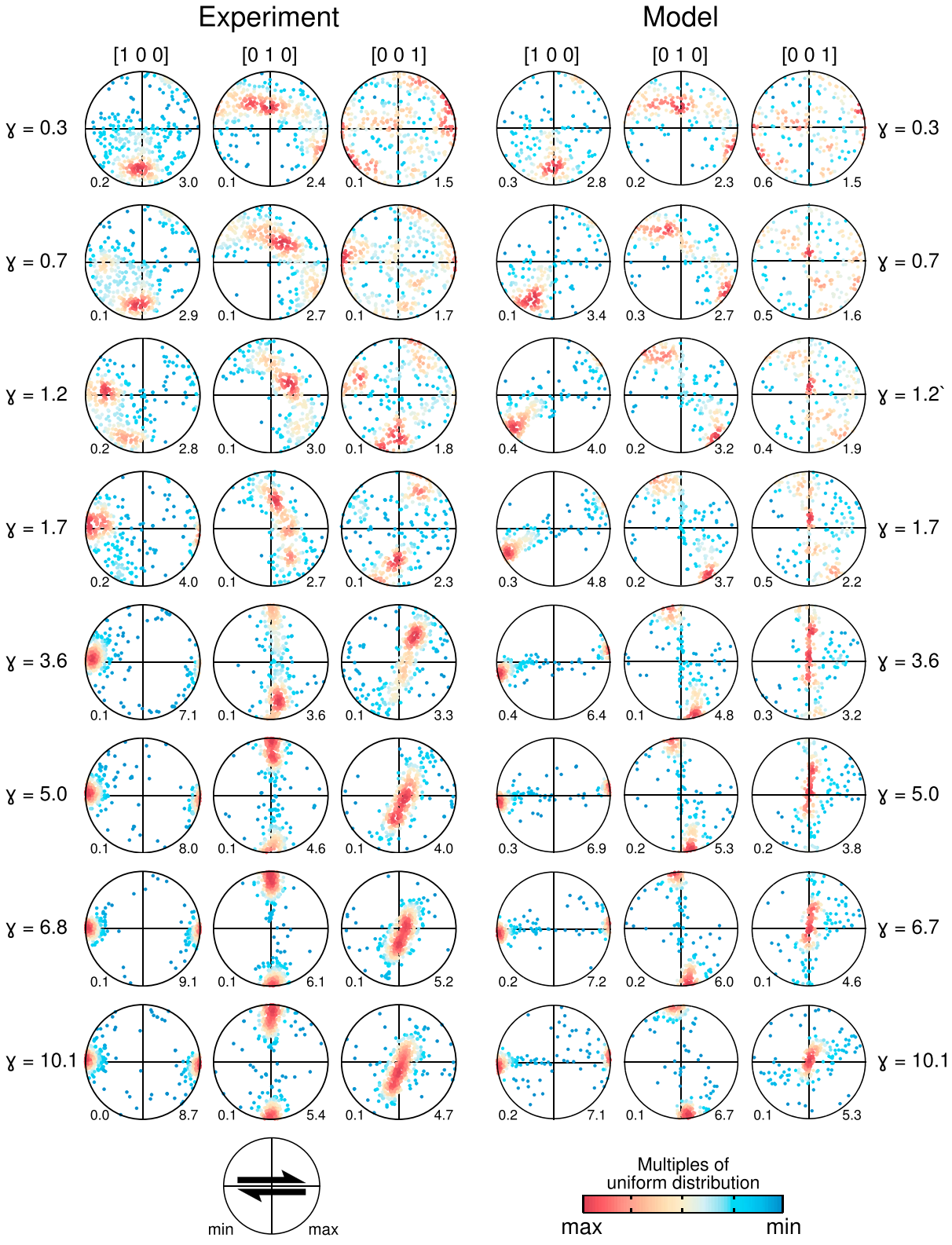

Figure 6. Comparison between observed textures and simulated textures as a function of the accumulated shear strain, γ. Observed textures are from sample PT0718 [*Hansen et al.*, 2016], which was deformed in extension prior to deformation in torsion. The simulated textural evolution was calculated using as an input the texture from the lowest-strain portion of sample PT0718. Individual points indicate grain orientations, and the color scale refers to the value of the orientation distribution function at that orientation. An animation of these data is included in the supporting information (Movie S1).

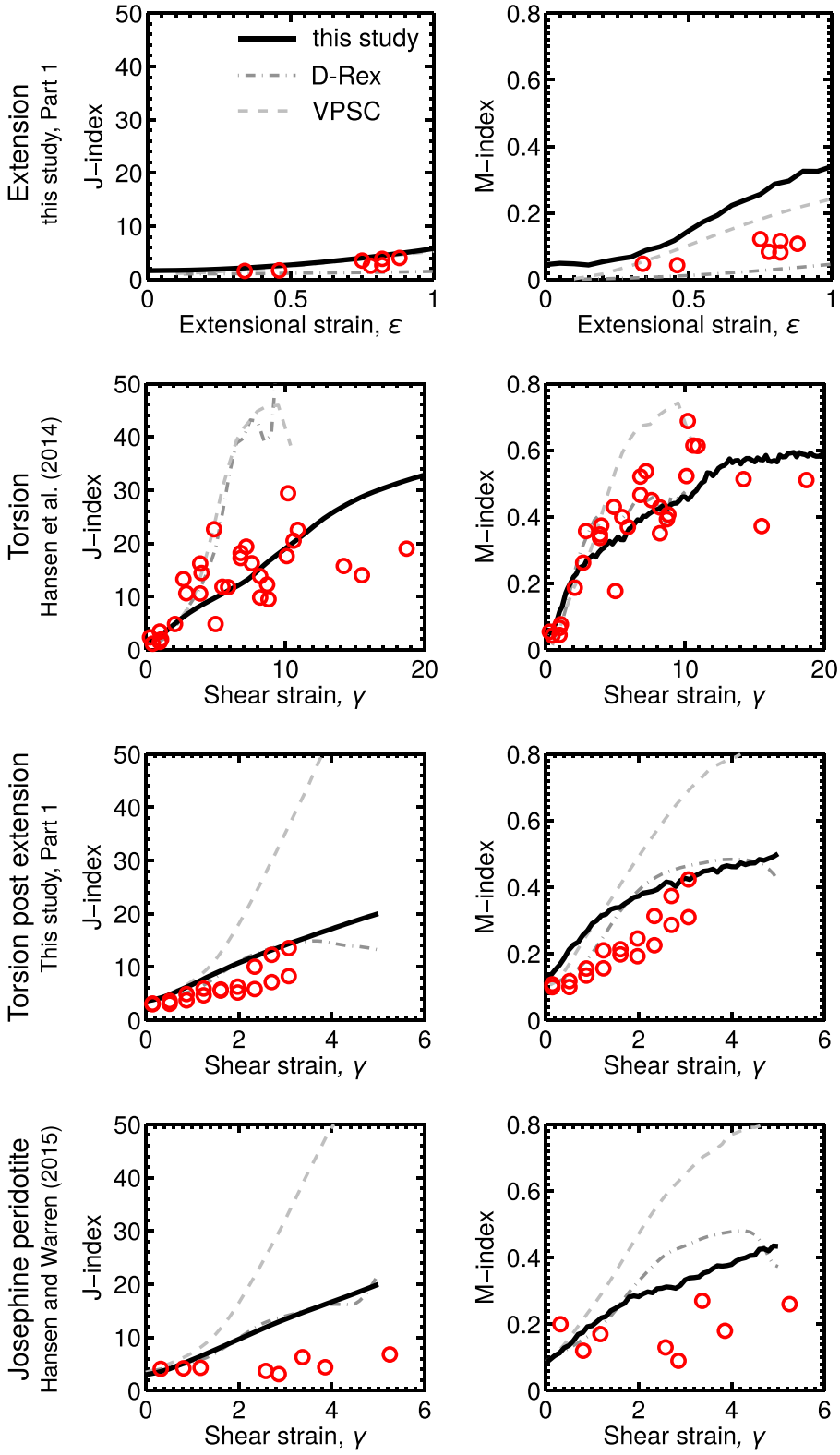

Figure 7. Comparison of texture strength from deformation experiments (circles) and numerical simulations (lines). Texture strength is measured with the J-index and the M-index. Experimental data are taken from extension experiments and subsequent torsion experiments presented in Part 1 of this study [*Hansen et al.*, 2016], torsion experiments with no initial texture [*Hansen et al.*, 2014], and naturally deformed dunites from the Josephine Peridotite [*Hansen and Warren*, 2015]. An animation of these data represented in pole figures is included in the supporting information (Movie S2).

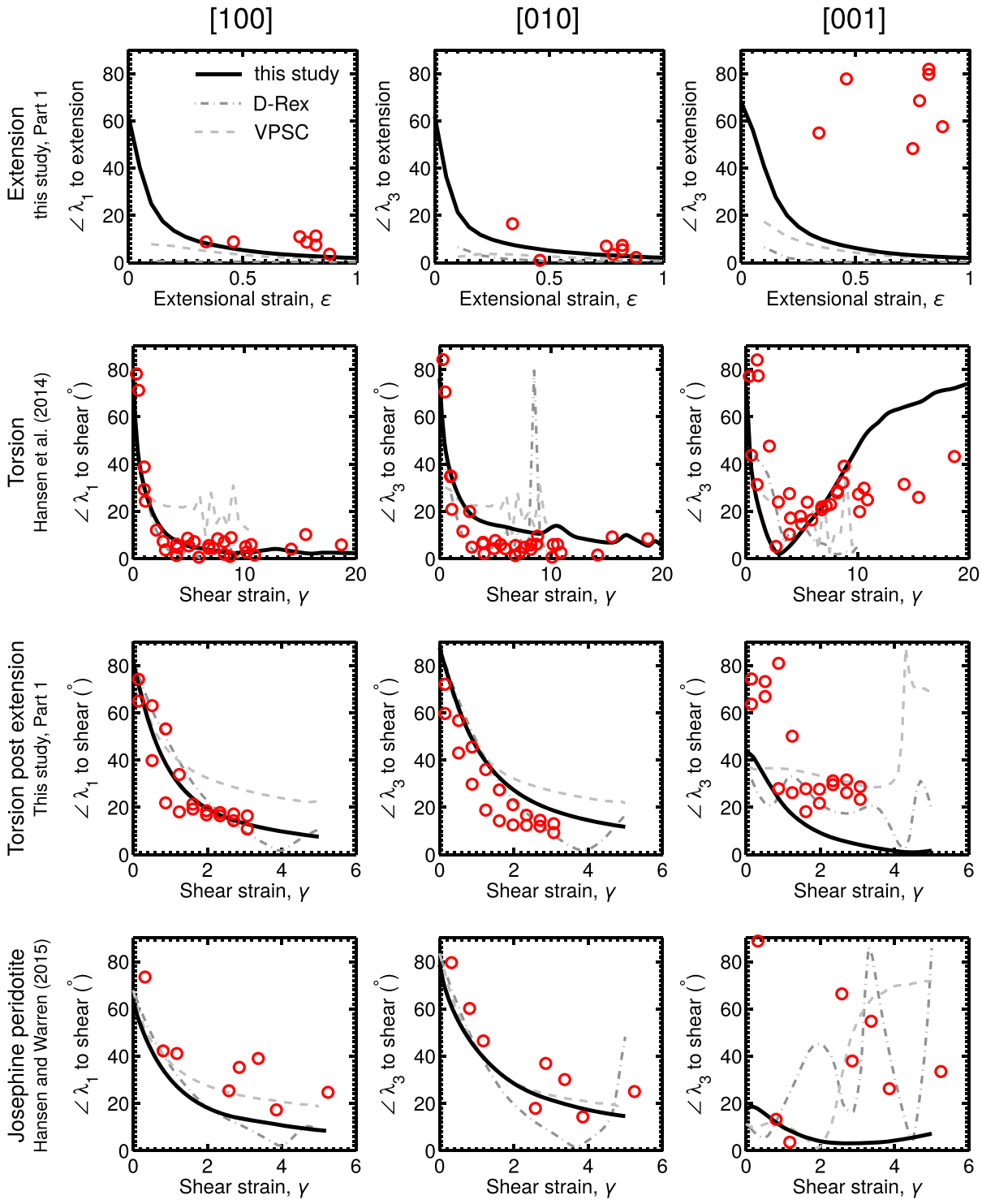

Figure 8. Comparison of texture orientation from deformation experiments (circles) and numerical simulations (lines). Data sources are as in Figure 7. Texture orientation is described with the eigenvectors of the orientation tensor for each axis distribution. For [100] axes, $\angle\lambda_1$ describes the angle between the shear direction and the dominant axis direction. For [010] and [001] axes, $\angle\lambda_3$ describes the angle between shear direction and the normal to the dominant girdle of axes. An animation of these data represented in pole figures is included in the supporting information (Movie S2).

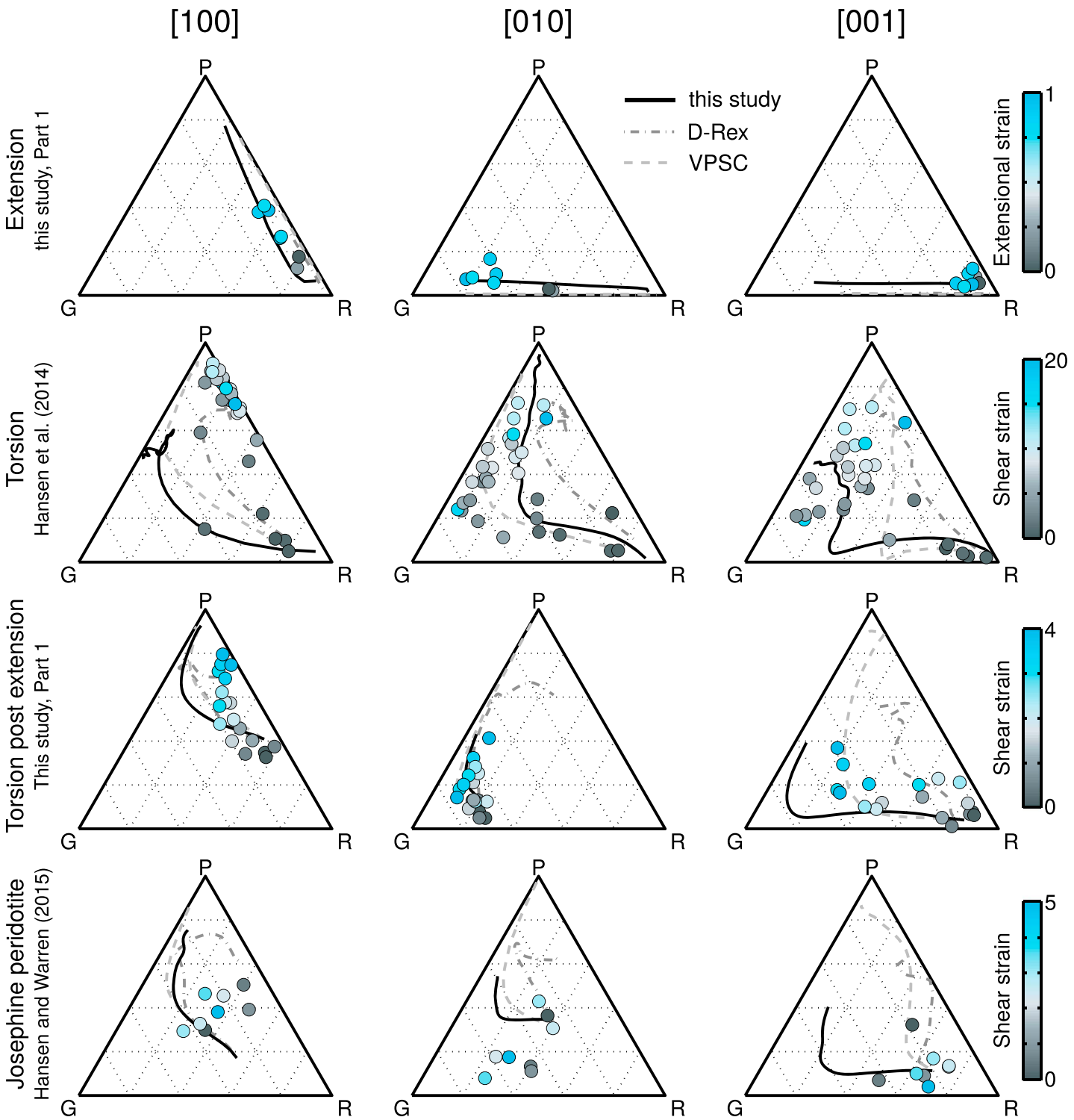

Figure 9. Comparison of texture shape from deformation experiments (circles) and numerical simulations (lines). Data sources are as in Figure 7. *P*, *G*, and *R* refer to the point, girdle, and random components of the axis distributions and are derived from the eigenvalues of the orientation tensor as described in the text. An animation of these data represented in pole figures is included in the supporting information (Movie S2).

change in the average orientation (Figure 8), regardless of whether the sample had an initially uniform texture or was initially deformed in extension. The simulations also reproduce the progressive girdling of [010] and [001] axes at low strains (Figure 9). Although the magnitude of girdling observed at intermediate strains in the experiments is higher than is observed in the simulations, the simulations do predict a transition to more point-like distributions of [010] and [001] axes at higher strains, as first described by *Hansen et al*. [2014].

Finally, simulated textures are compared to textures measured in dunites [*Hansen and Warren*, 2015] from a shear zone in the Josephine Peridotite (southwest Oregon). The initial texture used in the simulation was taken from a sample outside of the mapped shear zone (3923J01 [*Warren et al*., 2008]). Again, good agreement is found between simulations and textures, especially for the rate of change of the different texture characteristics. However, the simulation overpredicts the degree of girdling of [010] and [001] axes (Figure 9).

4. Discussion

4.1. Comparisons of Models and Observations

4.1.1. Mechanical Comparison

The pseudo-Taylor model is able to reproduce our experimental data set within error, while the Sachs model is unable to reproduce the measured anisotropy (Figure 3). It is worth exploring, then, potential reasons that the Sachs model is unable to reproduce the measured anisotropy. Because we empirically determine the best values of τ_o, the absolute strain rates and the magnitude of anisotropy are less important in evaluating the suitability of any particular model. Rather, it is the relative "sign" of anisotropy that is relevant. The pseudo-Taylor model correctly predicts that (1) during extension, samples with textures previously formed in torsion are stronger than those that are untextured, which are stronger than those with textures previously formed in extension and that (2) the converse is true during torsion. These statements are not true of the Sachs model. The Sachs model can be tuned such that the relative strengths are correctly predicted in extension, as exhibited in Figure 3a. However, it cannot be simultaneously tuned to predict that in torsion, samples with textures formed in torsion are weaker than hot-pressed samples (Figure 3c).

The difference between the responses of the two models likely results from the differences in fundamental constraints on grain interactions. The Sachs model is defined by each grain experiencing the same stress without constraints to maintain strain compatibility. Thus, the deformation in most grains is predicted to be primarily due to slip on the most favorably oriented slip system. The Sachs model therefore estimates the fastest strain rates for individual grains, and favorably oriented grains dominate the macroscopic strain rate. The pseudo-Taylor model requires each grain to follow the macroscopic strain rate tensor, which requires activation of multiple slip systems in most orientations. Thus, the strongest slip systems tend to dominate grain behavior, and the poorly oriented grains dominate the macroscopic stress.

It is therefore not surprising that samples with textures formed in torsion react very differently in the two models. Samples deformed to high strains in torsion form point maxima of [100], [010], and [001] axes (Figure 2). In torsion, many grains are favorably aligned for high resolved shear stresses on (010)[100]. In the Sachs model, this situation leads to behavior controlled by those well-oriented grains. However, in samples that do not exhibit strong textures, many grains are still oriented for large resolved shear stresses on the available slip systems, including the apparently weaker (001)[100]. These grains control the macroscopic response, and therefore the aggregate is similarly weak (or more so) than the sample with textures formed in torsion. The converse is true with the pseudo-Taylor model, in which very few grains are in orientations favorable for slip in samples previously deformed in torsion relative to those that have only been hot pressed.

Although the pseudo-Taylor model best reproduces the results from our experiments, it does not reproduce the data from samples initially deformed in extension and subsequently deformed in torsion (blue data in Figure 3d). Instead, the pseudo-Taylor model predicts a response in these samples similar to that of samples that have only been hot pressed (isotropic case). We suggest that this result arises from the nature of the textures formed in extension. Small circles of [010] and [001] axes resulting from extensional deformation (Figure 2) result in many grains in both favorable and unfavorable orientations for subsequent torsion. Grains with [010] or [001] aligned with the principal compressive stress have low resolved shear stresses on the available slip systems, whereas grains with those axes at high angles to the principal compressive

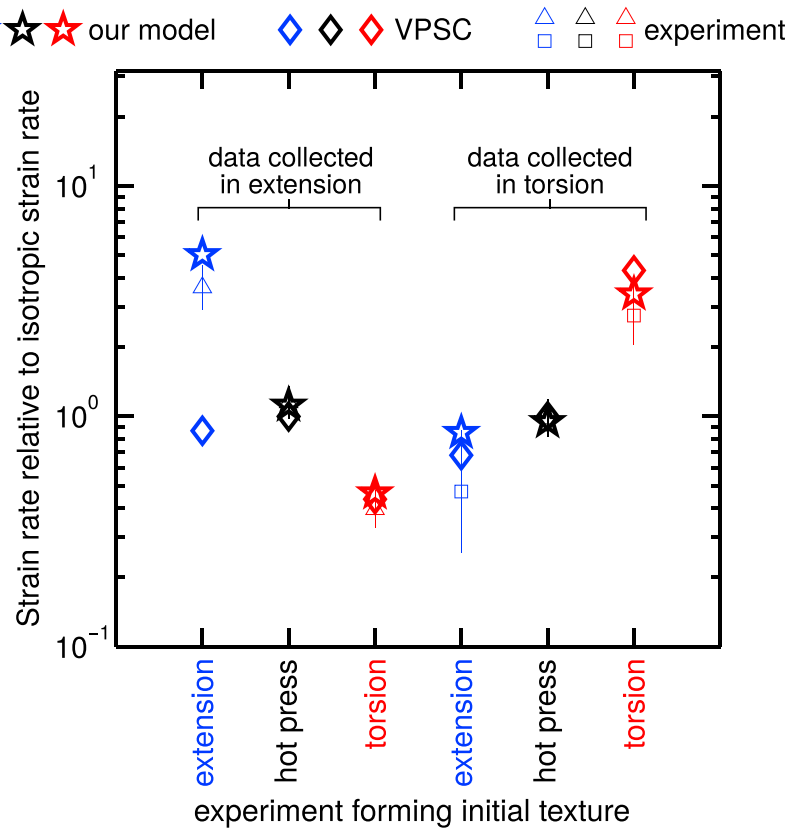

Figure 10. Comparison between normalized strain rates from experiments and models. Data are colored according to the type of experiment that was used to form the initial texture. Representative textures are presented in Figure 2. Data on the left side of the plot correspond to mechanical data measured in extension experiments. Data on the right side of the plot correspond to mechanical data measured in torsion experiments. Experimental strain rates and strain rates from our model (pseudo-Taylor) are normalized by the strain rates predicted by the isotropic flow law for Fo_{50} [*Hansen et al.*, 2012b] at the given conditions. Error bars for the experiments are one standard deviation. Strain rates for VPSC simulations are normalized by the strain rates predicted by VPSC simulations for aggregates with textures formed during hot pressing.

stress have high resolved shear stresses on the available slip systems. The small-circle girdles necessitate that relatively equal proportions of poorly and favorably oriented grains will be present, and therefore the macroscopic behavior is similar to that in the isotropic case.

The mechanical data for samples initially deformed in extension and subsequently deformed in tension (blue data in Figure 3d) have enough scatter that they cannot be statistically distinguished from the data collected for hot-pressed samples (black data in Figure 3d). This point is made clear in Figure 10, which demonstrates that the modeled response is within one standard deviation of the measured response. However, experiments on samples with textures formed in extension exhibit a mean strain rate that is slower than the mean determined for hot-pressed samples. If this relationship holds true, it suggests that processes other than anisotropy in the strength of slip systems (e.g., anisotropy in sliding velocities on grain boundaries) influence the macroscopic behavior.

The observation that the pseudo-Taylor model best reproduces our observations has several important implications for understanding the underlying microphysical deformation mechanisms. In neither the Sachs nor the pseudo-Taylor model do we fully satisfy strain compatibility due to the lack of slip systems in olivine. This point has been made by many previous authors [*Hirth and Kohlstedt*, 2003; *Kaminski et al.*, 2004; *Lebensohn et al.*, 2010; *Detrez et al.*, 2015]. We emphasize that the von Mises criterion requires five independent slip systems for homogeneous deformation. The criterion can be relaxed if stresses and strains are heterogeneously distributed below the grain scale, for which only four slip systems are required for macroscopically homogeneous deformation [*Hutchinson*, 1976; *Castelnau et al.*, 2008]. With only three independent

slip systems, olivine still requires processes in addition to dislocation slip to further relax the von Mises criterion. Potential processes include dislocation climb [e.g., *Goetze and Kohlstedt*, 1973; *Lebensohn et al*., 2010], dynamic recrystallization [e.g., *Kaminski et al*., 2004], and the translation of neighboring grains in association with grain boundary defects [*Hirth and Kohlstedt*, 2003; *Cordier et al*., 2014]. The strain rates predicted to arise solely from dislocation climb [*Nix et al*., 1971] are negligible due to slow Si self-diffusion in olivine [e.g., *Fei et al*., 2012]. Likewise, it is not yet established if significant strains can be produced through grain boundary migration in olivine (although subgrain boundary migration has been demonstrated to produce strain in aluminum [*Exell and Warrington*, 1972] and halite [*Guillope and Poirier*, 1979]). Thus, translation of neighboring grains (e.g., grain boundary sliding) is generally the favored mechanism for relaxing the von Mises criterion in olivine [*Hirth and Kohlstedt*, 1995, 2003]. The Sachs model effectively removes all compatibility constraints, which would correspond to fully relaxing the von Mises criterion. The better applicability of the pseudo-Taylor model to our data therefore implies that the von Mises criterion is only partially relaxed, and any additional strain resulting explicitly from sliding on boundaries is only produced as necessary. Furthermore, the apparent necessity to activate multiple slip systems in each grain is supported by the correspondence between the activation energy and oxygen fugacity dependence of creeping natural polycrystalline samples (Åheim dunite) [*Keefner et al*., 2011] and those of single crystals orientated to activate the hard slip system, (010)[001] [*Bai et al*., 1991].

Although our calibrated mechanical model can reasonably reproduce the mechanical data, it is also worth comparing our model and data to existing models for olivine deformation. We focus on a comparison with VPSC [e.g., *Lebensohn and Tomé*, 1993; *Tommasi et al*., 2000]. Figure 10 presents mechanical data from our experiments and model as well as the response predicted by the VPSC model. For these simulations, we use the VPSC tangent linearization method (in which $\beta = 1$) and slip system activities for high-temperature deformation [see *Tommasi et al*., 2000, Table 2]. In general, the VPSC results are in agreement with the experimental data and our model output. The biggest discrepancy lies in the results for samples with a preexisting texture formed by extension with additional, subsequent extensional deformation (far left data points in Figure 10). In this case, the VPSC results dramatically underpredict the measured strain rates. Our interpretation of this discrepancy is that in VPSC simulations, texture generated by extension is insufficient to affect the relative strain rate, because the texture strength is relatively weak ($M = 0.1$, Figure 7) in comparison to the texture strength generated in torsion ($M = 0.5$–0.6, Figure 7). This observation implies that samples with textures formed in extension are effectively isotropic (compare all blue data in Figure 10). This result is not borne out by our experimental results, which yield an anisotropy in strain rate of a factor of ~8. Thus, we conclude that the pseudo-Taylor model represents a significant improvement over the VPSC simulations in reproducing the experimentally measured anisotropy in viscosity.

4.1.2. Textural Comparison

Our textural evolution model also reproduces the experimental observations well, especially considering the simplicity of the model setup. As illustrated in Figures 7–9, the model reproduces the evolution in texture strength, orientation, and symmetry for a variety of deformation geometries and complex strain histories. In addition, we examine the ability of the model to reproduce the textural evolution observed in a natural shear zone in the Josephine Peridotite [*Hansen and Warren*, 2015]. Our model and experimental data are also compared to the predictions of two widely used textural evolution models, VPSC [e.g., *Lebensohn and Tomé*, 1993; *Tommasi et al*., 2000] and D-Rex [*Kaminski and Ribe*, 2001; *Kaminski et al*., 2004].

The evolution of texture strength in the experiments is much better approximated by our model than by either VPSC or the D-Rex simulations, which both tend to overpredict texture strength (Figure 7). In the simulations of torsion with our model, the texture strength reaches approximately steady state values of the J-index and M-index of ~30 and ~0.6, respectively, at shear strains greater than ~15. These values are comparable to the upper limit of those observed in naturally deformed rocks [*Ismaïl and Mainprice*, 1998]. Experimental data from torsion of dry aggregates of olivine at high strain [*Hansen et al*., 2014] do exhibit weaker textures than our model predicts. However, samples deformed to the highest strains also exhibit the finest grain sizes for which texture strength is weakened due to the increased contribution of secondary grain size sensitive deformation mechanisms [*Hansen et al*., 2014]. The results from simulations of texture in samples deformed in torsion for both VPSC and D-Rex exhibit significantly larger values of the J-index than observed in our model or in experiments, even at shear strains of 10. In general, VPSC yields stronger textures than D-Rex and continues increasing without reaching stable values (Figure 7). An animation comparing the

textural evolution during torsion in our model, D-Rex, and VPSC is included in the supporting information (Movie S2). For experiments in extension, VPSC is in agreement with both our model and the experimental data, whereas D-Rex underpredicts the texture strength. For experiments in torsion subsequent to extension, VPSC severely overpredicts the texture strength, whereas D-Rex is in agreement with our model and experimental data. In our simulations of the data from samples collected from a natural shear zone [*Hansen and Warren*, 2015], all of the models overpredict the texture strength, although our model and D-Rex yield weaker textures than VPSC. The high texture strengths characteristic of VPSC models have been recently addressed in new parameterizations that simulate the effects of dynamic recrystallization on textural evolution [*Signorelli and Tommasi*, 2015].

We suggest that the subdued strengthening of the crystallographic textures in the model presented here relative to those in VPSC and D-Rex is a result of the driving force for grain rotation being determined with the director method [*Mühlhaus et al*., 2002, 2004]. *Lev and Hager* [2008a] compared several textural evolution models and noted that the director method, although only a 2-D representation of anisotropy, particularly excelled at representing texture development at large strains. Previous implementations of the director method were parameterized such that the director is normal to a plane of weakness and rotates to align the plane of weakness with the shear plane. This formulation implies that the anisotropy of each grain has relatively high symmetry (i.e., transversely isotropic). We circumvent this issue and extend the method to 3-D by suggesting that the director aligns with the flow direction and by constraining the axis of rotation with the available slip systems. Thus, our approach combines the stability of the director method at large strains with slip system anisotropy present in micromechanical models. The subdued strengthening of the texture in our model is in generally good agreement with that in D-Rex using the calibrated parameters from *Boneh et al*. [2015]. This agreement increases our confidence that our results from deformation experiments on Fo_{50} olivine are applicable to olivine compositions more typical of Earth's upper mantle.

There are also some key differences between our model and the VPSC and D-Rex approaches in terms of the orientation of the simulated textures. Average orientations for [100], [010], and [001] axes are presented in Figure 8. The average orientation of the [100] axes (the λ_1 eigenvector) gradually approaches the shear direction in torsion or the extension direction in extension for all of the simulations and the experimental observations. The rates of this change in orientation are well reproduced by all except the VPSC model, which exhibits significantly slower evolution than the other models in torsion. This behavior is likely due to the absence of an explicit scheme for simulating dynamic recrystallization in our VPSC model, as has been attempted in some recent models [*Signorelli and Tommasi*, 2015]. The VPSC simulations also begin to exhibit some numerical instability at shear strains of ~5. A similar set of observations is made for the normal to the girdle of [010] axes (the λ_3 eigenvector). The average orientation of the normal to the girdle of the [001] axes is particularly interesting. In torsion, the VPSC and D-Rex models predict that λ_3 approaches the shear direction. However, our samples exhibit a girdle that is not normal to the shear direction (Figure 6), and our textural evolution model exhibits similar behavior (Figure 8). In extension, however, our samples exhibit small-circle girdles of [001] axes leading to orientations of λ_3 at a high angle to the extension direction. This feature is not replicated by any of the models (Figure 8), and the mechanism for its formation remains unclear.

The shapes of the individual orientation distributions are assessed with values of *P*, *G*, and *R*. The ternary diagrams presented in Figure 9 illustrate that our textural evolution model predicts significantly more girdling of [001] axes than the other models. This degree of girdling is in good agreement with the experimental data from torsion experiments, but it overpredicts the amount of girdling in the data from the natural shear zone in the Josephine Peridotite. In contrast, D-Rex significantly underpredicts the amount of girdling in all scenarios involving simple shear. Thus, although this formulation of D-Rex does well at predicting the strength of the texture, it struggles to replicate shape of the texture. VPSC produces a magnitude of girdling that is intermediate to D-Rex and our model.

All models overpredict the amount of girdling of [001] axes during extension (Figure 9). This difference likely results from the small-circle girdles in the experiments, which lead to higher values of *R* at the expense of values of *G*. The [100] axes form point maxima in the experiments, which is reasonably reproduced by all models. In torsion, however, the models all predict more girdling of [100] axes than is observed. It is not immediately clear why this difference exists. This [100] girdling is most pronounced in

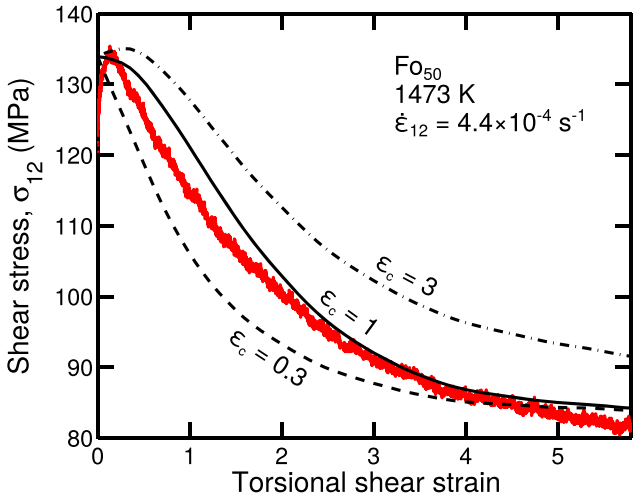

Figure 11. Comparison of (red) measured stress-strain curve from a torsion experiment (PT0552 [*Hansen et al*., 2012b]) compared to (black) predicted curves resulting from coupling the mechanical and textural evolution models presented in this study. Observations and calculations are for constant temperature and constant strain rate. Calculations also include grain size reduction based on equation number (10). Three different simulated curves are presented, each computed using a different value of the characteristic strain for grain size evolution, ε_c.

our model and least pronounced in D-Rex, suggesting that recrystallization processes are important in generating strong [100] point maxima.

We emphasize here that our relatively simple textural evolution model does well at reproducing the experimental results and often does better than existing models. Furthermore, our model is stable to large deformation and, therefore, can be more robustly incorporated into large-scale geodynamic models.

4.2. Coupled Textural and Mechanical Model

The mechanical and textural models developed here can be coupled so that mechanical behavior and texture evolve dynamically. This coupling is desirable for geodynamic simulations in which changes in the orientation and magnitude of viscous anisotropy affect the viscous flow patterns and the rock textures that result from them. In the mantle, such systems may involve plate motions [e.g., *Becker and Kawakatsu*, 2011], corner flow at ridges [e.g., *Castelnau et al*., 2009], subduction [e.g., *Lev and Hager*, 2011], and convective instability beneath the lithosphere [*Lev and Hager*, 2008b].

In Figure 11, we compare the results of the coupled model to the results from a torsion test on untextured Fo_{50} from *Hansen et al*. [2012b] (sample PT0552). Because the dominant deformation mechanism in these aggregates is grain size sensitive, grain size evolution needs to be taken into account to allow comparison of the simulated and measured mechanical evolution. We use the simple grain size evolution model implemented by *Hansen et al*. [2012b] to model grain size reduction during torsion of Fo_{50}. The rate of change in grain size can be described as

$$\dot{d} = \frac{\dot{\varepsilon}(d_{ss} - d)}{\varepsilon_c}, \tag{10}$$

where $\dot{\varepsilon}$ is the von Mises equivalent strain rate, ε_c is a critical strain for grain size evolution that phenomenologically approximates the dependence of the degree of dynamic recrystallization on the total accumulated strain [*Braun et al*., 1999], and d_{ss} is the steady state grain size (given by equation (5) and reported parameter values in *Hansen et al*. [2012b]). With some tuning of ε_c, we are able to reproduce the magnitude and timescale of the observed stress drop.

Hansen et al. [2012b] employed an equation similar to (10) to simplistically describe textural evolution. They had to assume a value for the critical strains for both grain size evolution and textural evolution because these two processes both contribute to weakening and their timescales of evolution could not be determined separately. They found that a value of $\varepsilon_c = 1$ for both grain size and textural evolution reasonably replicated the data. Here we have calibrated our micromechanical model to reproduce the more recent observations of textural evolution, and therefore we can independently constrain the value of ε_c for grain size evolution. Comparison of simulated data and experimental data from sample PT0552 demonstrate that good agreement is found with a critical strain for grain size evolution of $\varepsilon_c = 1$ (Figure 11). Thus, as assumed by *Hansen et al*. [2012b], the textural evolution appears to operate on a similar timescale as grain size evolution.

This coupled model provides a new tool for capturing anisotropy and its evolution in large-scale flow models. However, because the pseudo-Taylor model uses strain rate as an input, the coupled model will be best suited to flow models that calculate the stress as a response to an imposed strain rate [e.g., *Castelnau et al*., 2009].

Our coupled model can still be incorporated in flow models that calculate the strain rate as a function of an imposed stress, but an iterative approach will need to be taken at each time step to find the strain rate that, when used as an input to the pseudo-Taylor model, yields the imposed stress state. Optimized implementation of the coupled model in different flow scenarios will be the subject of future work.

5. Conclusions

A micromechanical model that predicts mechanical and textural evolution for large and complex deformations of olivine aggregates is distinctly needed in the geodynamics community. With recently acquired data sets, we calibrate two new models of olivine deformation. The first calculates the stress tensor necessary to deform an aggregate of grains according to a given macroscopic strain rate tensor and a distribution of grain orientations. The second calculates the evolution of that distribution of grain orientations for an arbitrary strain history. We determined the best fit model parameters quantitatively with an inversion procedure based on a genetic algorithm. Our best fit models are able to reasonably reproduce the experimentally derived mechanical behavior and textural evolution.

This work represents a key step forward in incorporating viscous anisotropy into large-scale geodynamic models. As demonstrated through quantitative comparison, our models are better at predicting mechanical anisotropy than previously published micromechanical models. Our models also represent a major improvement over previous models for textural evolution, better capturing the shape of the texture, the strength of the texture, and the timescale of the textural evolution. Importantly, our textural evolution model is also stable to very large strains, whereas previous models are generally limited to small deformations (e.g., shear strains <10). Furthermore, our models can be coupled and used to reproduce the mechanical evolution associated with the evolving crystallographic texture. This set of models represents a new geodynamic tool that will allow easy incorporation of viscous anisotropy into large-scale geodynamic simulations.

Acknowledgments
The concepts and interpretation presented here benefited greatly from conversations with Greg Hirth, Andréa Tommasi, Andrew Turner, and David Wallis. The manuscript was improved by constructive comments from Luiz Morales and an anonymous reviewer. All data presented in this work are available by directly contacting the corresponding author. This work was funded by John Fell Fund grant 123/718 to L.N.H.; Natural Environment Research Council grant NE/M000966/1 to L.N.H.; National Science Foundation grants EAR-1151241 to C.P.C., EAR-1141795 to P.S., EAR-1255620 to J.M.W., and EAR-1520647 to D.L.K.; and the Research Council of Norway's Centres of Excellence project 223272.

References

Bachmann, F., R. Hielscher, and H. Schaeben (2010), Texture analysis with MTEX—Free and open source software toolbox, *Diffus. Defect Data, Part B*, *160*, 63–68.

Bai, Q., S. J. Mackwell, and D. L. Kohlstedt (1991), High-temperature creep of olivine single crystals 1. Mechanical results for buffered samples, *J. Geophys. Res.*, *96*, 2441–2463, doi:10.1029/90JB01723.

Becker, T. W., and H. Kawakatsu (2011), On the role of anisotropic viscosity for plate-scale flow, *Geophys. Res. Lett.*, *38*, L17307, doi:10.1029/2011GL048584.

Bishop, J. F. W., and R. Hill (1951), XLVI. A theory of the plastic distortion of a polycrystalline aggregate under combined stresses, *Philos. Mag.*, *42*(327), 414–427.

Blackman, D. K., H.-R. Wenk, and J. M. Kendall (2002), Seismic anisotropy of the upper mantle 1. Factors that affect mineral texture and effective elastic properties, *Geochem. Geophys. Geosyst.*, *3*(9), 8601, doi:10.1029/2001GC000248.

Bogacki, P., and L. F. Shampine (1989), A 3(2) pair of Runge-Kutta formulas, *Appl. Math. Lett.*, *2*(4), 321–325, doi:10.1016/0893-9659(89)90079-7.

Boneh, Y., and P. Skemer (2014), The effect of deformation history on the evolution of olivine CPO, *Earth Planet. Sci. Lett.*, *406*, 213–222.

Boneh, Y., L. F. G. Morales, E. Kaminski, and P. Skemer (2015), Modeling olivine CPO evolution with complex deformation histories: Implications for the interpretation of seismic anisotropy in the mantle, *Geochem. Geophys. Geosyst.*, *16*, 3436–3455, doi:10.1002/2015GC005964.

Braun, J., J. Chéry, A. Poliakov, D. Mainprice, A. Vauchez, A. Tomassi, and M. Daignières (1999), A simple parameterization of strain localization in the ductile regime due to grain size reduction: A case study for olivine, *J. Geophys. Res.*, *104*, 25,167–25,181, doi:10.1029/1999JB900214.

Bunge, H.-J. (2013), *Texture Analysis in Materials Science: Mathematical Methods*, Butterworths, London.

Castelnau, O., D. Blackman, R. Lebensohn, and P. P. Castañeda (2008), Micromechanical modeling of the viscoplastic behavior of olivine, *J. Geophys. Res.*, *113*, B09202, doi:10.1029/2007JB005444.

Castelnau, O., D. K. Blackman, and T. W. Becker (2009), Numerical simulations of texture development and associated rheological anisotropy in regions of complex mantle flow, *Geophys. Res. Lett.*, *36*, L12304, doi:10.1029/2009GL038027.

Christensen, U. R. (1987), Some geodynamical effects of anisotropic viscosity, *Geophys. J. Int.*, *91*(3), 711–736.

Conrad, C. P., S. Bilek, and C. Lithgow-Bertelloni (2004), Great earthquakes and slab pull: Interaction between seismic coupling and plate–slab coupling, *Earth Planet. Sci. Lett.*, *218*(1–2), 109–122, doi:10.1016/S0012-821X(03)00643-5.

Cordier, P., S. Demouchy, B. Beausir, V. Taupin, F. Barou, and C. Fressengeas (2014), Disclinations provide the missing mechanism for deforming olivine-rich rocks in the mantle, *Nature*, *507*(7490), 51–56, doi:10.1038/nature13043.

Detrez, F., O. Castelnau, P. Cordier, S. Merkel, and P. Raterron (2015), Effective viscoplastic behavior of polycrystalline aggregates lacking four independent slip systems inferred from homogenization methods; application to olivine, *J. Mech. Phys. Solids*, *83*, 199–220, doi:10.1016/j.jmps.2015.05.022.

Durham, W. B., and C. Goetze (1977), Plastic flow of oriented single crystals of olivine 1. Mechanical data, *J. Geophys. Res.*, *82*, 5737–5753, doi:10.1029/JB082i036p05737.

Exell, S. F., and D. H. Warrington (1972), Sub-grain boundary migration in aluminium, *Philos. Mag.*, *26*(5), 1121–1136, doi:10.1080/14786437208227368.

Fei, H., C. Hegoda, D. Yamazaki, M. Wiedenbeck, H. Yurimoto, S. Shcheka, and T. Katsura (2012), High silicon self-diffusion coefficient in dry forsterite, *Earth Planet. Sci. Lett.*, *345–348*, 95–103, doi:10.1016/j.epsl.2012.06.044.

Forrest, S. (1993), Genetic algorithms: Principles of natural selection applied to computation, *Science*, *261*(5123), 872–878, doi:10.1126/science.8346439.

Goetze, C., and D. L. Kohlstedt (1973), Laboratory study of dislocation climb and diffusion in olivine, *J. Geophys. Res.*, *78*, 5961–5971, doi:10.1029/JB078i026p05961.
Goldberg, D. E. (1989), *Genetic Algorithms in Search, Optimization and Machine Learning*, 1st ed., Addison-Wesley Longman Co., Inc., Boston, Mass.
Groves, G., and A. Kelly (1963), Independent slip systems in crystals, *Philos. Mag.*, *8*(89), 877–887.
Guillope, M., and J. P. Poirier (1979), Dynamic recrystallization during creep of single-crystalline halite: An experimental study, *J. Geophys. Res.*, *84*, 5557–5567, doi:10.1029/JB084iB10p05557.
Han, D., and J. Wahr (1997), An analysis of anisotropic mantle viscosity, and its possible effects on post-glacial rebound, *Phys. Earth Planet. Inter.*, *102*(1–2), 33–50, doi:10.1016/S0031-9201(96)03268-2.
Hansen, L. N., and J. M. Warren (2015), Quantifying the effect of pyroxene on deformation of peridotite in a natural shear zone, *J. Geophys. Res. Solid Earth*, *120*, 2717–2738, doi:10.1002/2014JB011584.
Hansen, L. N., M. E. Zimmerman, and D. L. Kohlstedt (2012a), Laboratory measurements of the viscous anisotropy of olivine aggregates, *Nature*, *492*(7429), 415–418, doi:10.1038/nature11671.
Hansen, L. N., M. E. Zimmerman, and D. L. Kohlstedt (2012b), The influence of microstructure on deformation of olivine in the grain-boundary sliding regime, *J. Geophys. Res.*, *117*, B09201, doi:10.1029/2012JB009305.
Hansen, L. N., Y.-H. Zhao, M. E. Zimmerman, and D. L. Kohlstedt (2014), Protracted fabric evolution in olivine: Implications for the relationship among strain, crystallographic fabric, and seismic anisotropy, *Earth Planet. Sci. Lett.*, *387*, 157–168, doi:10.1016/j.epsl.2013.11.009.
Hansen, L. N., J. M. Warren, M. E. Zimmerman, and D. L. Kohlstedt (2016), Viscous anisotropy of textured olivine aggregates, part 1: Measurement of the magnitude and evolution of anisotropy, *Earth Planet. Sci. Lett.*, *445*, 92–103, doi:10.1016/j.epsl.2016.04.008.
Hearn, E. H., E. D. Humphreys, M. Chai, and J. M. Brown (1997), Effect of anisotropy on oceanic upper mantle temperatures, structure, and dynamics, *J. Geophys. Res.*, *102*, 11,943–11,956, doi:10.1029/97JB00506.
Hedjazian, N., and E. Kaminski (2014), Defining a proxy for the interpretation of seismic anisotropy in non-Newtonian mantle flows, *Geophys. Res. Lett.*, *41*, 7065–7072, doi:10.1002/2014GL061372.
Hielscher, R., and H. Schaeben (2008), A novel pole figure inversion method: Specification of the MTEX algorithm, *J. Appl. Crystallogr.*, *41*(6), 1024–1037.
Hirth, G., and D. Kohlstedt (2003), Rheology of the upper mantle and the mantle wedge: A view from the experimentalists, in *Inside the Subduction Factory*, *Geophys. Monogr. Ser.*, vol. 138, edited by J. Eiler, pp. 83–105, AGU, Washington, D. C.
Hirth, G., and D. L. Kohlstedt (1995), Experimental constraints on the dynamics of the partially molten upper mantle: 2. Deformation in the dislocation creep regime, *J. Geophys. Res.*, *100*, 15,441–15,449, doi:10.1029/95JB01292.
Honda, S. (1986), Strong anisotropic flow in a finely layered asthenosphere, *Geophys. Res. Lett.*, *13*, 1454–1457, doi:10.1029/GL013i013p01454.
Hutchinson, J. W. (1976), Bounds and self-consistent estimates for creep of polycrystalline materials, *Proc. R. Soc. London, Ser. A*, *348*(1652), 101–127, doi:10.1098/rspa.1976.0027.
Ismaïl, W. B., and D. Mainprice (1998), An olivine fabric database: An overview of upper mantle fabrics and seismic anisotropy, *Tectonophysics*, *296*(1–2), 145–157, doi:10.1016/S0040-1951(98)00141-3.
Kaminski, E., and N. Ribe (2001), A kinematic model for recrystallization and texture development in olivine polycrystals, *Earth Planet. Sci. Lett.*, *189*(3), 253–267.
Kaminski, É., N. M. Ribe, and J. T. Browaeys (2004), D-Rex, a program for calculation of seismic anisotropy due to crystal lattice preferred orientation in the convective upper mantle, *Geophys. J. Int.*, *158*(2), 744–752, doi:10.1111/j.1365-246X.2004.02308.x.
Karato, S. (1988), The role of recrystallization in the preferred orientation of olivine, *Phys. Earth Planet. Inter.*, *51*(1–3), 107–122, doi:10.1016/0031-9201(88)90029-5.
Keefner, J. W., S. J. Mackwell, D. L. Kohlstedt, and F. Heidelbach (2011), Dependence of dislocation creep of dunite on oxygen fugacity: Implications for viscosity variations in Earth's mantle, *J. Geophys. Res.*, *116*, B05201, doi:10.1029/2010JB007748.
King, S. D. (1995), Radial models of mantle viscosity: Results from a genetic algorithm, *Geophys. J. Int.*, *122*(3), 725–734, doi:10.1111/j.1365-246X.1995.tb06831.x.
Knoll, M., A. Tommasi, R. E. Logé, and J. W. Signorelli (2009), A multiscale approach to model the anisotropic deformation of lithospheric plates, *Geochem. Geophys. Geosyst.*, *10*, Q08009, doi:10.1029/2009GC002423.
Lebensohn, R. (2001), N-site modeling of a 3D viscoplastic polycrystal using fast Fourier transform, *Acta Mater.*, *49*(14), 2723–2737, doi:10.1016/S1359-6454(01)00172-0.
Lebensohn, R., and C. Tomé (1993), A self-consistent anisotropic approach for the simulation of plastic deformation and texture development of polycrystals: Application to zirconium alloys, *Acta Metall. Mater.*, *41*(9), 2611–2624.
Lebensohn, R., H.-R. Wenk, and C. Tomé (1998), Modelling deformation and recrystallization textures in calcite, *Acta Mater.*, *46*(8), 2683–2693.
Lebensohn, R. A., C. S. Hartley, C. N. Tomé, and O. Castelnau (2010), Modeling the mechanical response of polycrystals deforming by climb and glide, *Philos. Mag.*, *90*(5), 567–583, doi:10.1080/14786430903213320.
Lee, K.-H., Z. Jiang, and S. Karato (2002), A scanning electron microscope study of the effects of dynamic recrystallization on lattice preferred orientation in olivine, *Tectonophysics*, *351*(4), 331–341, doi:10.1016/S0040-1951(02)00250-0.
Lev, E., and B. H. Hager (2008a), Prediction of anisotropy from flow models: A comparison of three methods, *Geochem. Geophys. Geosyst.*, *9*, Q07014, doi:10.1029/2008GC002032.
Lev, E., and B. H. Hager (2008b), Rayleigh–Taylor instabilities with anisotropic lithospheric viscosity, *Geophys. J. Int.*, *173*(3), 806–814, doi:10.1111/j.1365-246X.2008.03731.x.
Lev, E., and B. H. Hager (2011), Anisotropic viscosity changes subduction zone thermal structure, *Geochem. Geophys. Geosyst.*, *12*, Q04009, doi:10.1029/2010GC003382.
Mises, R. V. (1928), Mechanik der plastischen Formänderung von Kristallen, *Z. Angew. Math. Mech.*, *8*(3), 161–185.
Mühlhaus, H., H. Moresi, and M. Cada (2004), Emergent anisotropy and flow alignment in viscous rock, in *Computational Earthquake Science Part II*, pp. 2451–2463, Springer, Basel, Switzerland.
Mühlhaus, H.-B., L. Moresi, B. Hobbs, and F. Dufour (2002), Large amplitude folding in finely layered viscoelastic rock structures, *Pure Appl. Geophys.*, *159*(10), 2311–2333, doi:10.1007/s00024-002-8737-4.
Nicolas, A., F. Boudier, and A. M. Boullier (1973), Mechanisms of flow in naturally and experimentally deformed peridotites, *Am. J. Sci.*, *273*(10), 853–876, doi:10.2475/ajs.273.10.853.
Nix, W. D., R. Gasca-Neri, and J. P. Hirth (1971), A contribution to the theory of dislocation climb, *Philos. Mag.*, *23*(186), 1339–1349, doi:10.1080/14786437108217006.

Pokharel, R., J. Lind, A. K. Kanjarla, R. A. Lebensohn, S. F. Li, P. Kenesei, R. M. Suter, and A. D. Rollett (2014), Polycrystal plasticity: Comparison between grain-scale observations of deformation and simulations, *Annu. Rev. Condens. Matter Phys.*, *5*(1), 317–346.

Ribe, N. M., and Y. Yu (1991), A theory for plastic deformation and textural evolution of olivine polycrystals, *J. Geophys. Res.*, *96*, 8325–8335, doi:10.1029/90JB02721.

Rutter, E., M. Casey, and L. Burlini (1994), Preferred crystallographic orientation development during the plastic and superplastic flow of calcite rocks, *J. Struct. Geol.*, *16*(10), 1431–1446.

Sachs, G. (1928), The plastic deformation mode of polycrystals, *Z. Ver. Dtsch. Ing.*, *72*, 734.

Signorelli, J., and A. Tommasi (2015), Modeling the effect of subgrain rotation recrystallization on the evolution of olivine crystal preferred orientations in simple shear, *Earth Planet. Sci. Lett.*, *430*, 356–366, doi:10.1016/j.epsl.2015.08.018.

Skemer, P., and L. N. Hansen (2016), Inferring mantle flow from seismic anisotropy: An experimental perspective, *Tectonophysics*, *668–669*, 1–14, doi:10.1016/j.tecto.2015.12.003.

Skemer, P., I. Katayama, Z. Jiang, and S. Karato (2005), The misorientation index: Development of a new method for calculating the strength of lattice-preferred orientation, *Tectonophysics*, *411*(1), 157–167.

Skemer, P., J. M. Warren, and G. Hirth (2012), The influence of deformation history on the interpretation of seismic anisotropy, *Geochem. Geophys. Geosyst.*, *13*, Q03006, doi:10.1029/2011GC003988.

Taylor, G. (1938), Plastic deformation of metals. 1, *J. Inst. Met.*, *62*, 307.

Tommasi, A. (1998), Forward modeling of the development of seismic anisotropy in the upper mantle, *Earth Planet. Sci. Lett.*, *160*(1–2), 1–13, doi:10.1016/S0012-821X(98)00081-8.

Tommasi, A., B. Tikoff, and A. Vauchez (1999), Upper mantle tectonics: Three-dimensional deformation, olivine crystallographic fabrics and seismic properties, *Earth Planet. Sci. Lett.*, *168*(1–2), 173–186, doi:10.1016/S0012-821X(99)00046-1.

Tommasi, A., D. Mainprice, G. Canova, and Y. Chastel (2000), Viscoplastic self-consistent and equilibrium-based modeling of olivine lattice preferred orientations: Implications for the upper mantle seismic anisotropy, *J. Geophys. Res.*, *105*, 7893–7908, doi:10.1029/1999JB900411.

Tommasi, A., M. Knoll, A. Vauchez, J. W. Signorelli, C. Thoraval, and R. Logé (2009), Structural reactivation in plate tectonics controlled by olivine crystal anisotropy, *Nat. Geosci.*, *2*(6), 423–427, doi:10.1038/ngeo528.

Vollmer, F. W. (1990), An application of eigenvalue methods to structural domain analysis, *Geol. Soc. Am. Bull.*, *102*(6), 786–791, doi:10.1130/0016-7606(1990)102<0786:AAOEMT>2.3.CO;2.

Warren, J. M., G. Hirth, and P. B. Kelemen (2008), Evolution of olivine lattice preferred orientation during simple shear in the mantle, *Earth Planet. Sci. Lett.*, *272*(3–4), 501–512, doi:10.1016/j.epsl.2008.03.063.

Zhang, S., and S. Karato (1995), Lattice preferred orientation of olivine aggregates deformed in simple shear, *Nature*, *375*(6534), 774–777, doi:10.1038/375774a0.

Zhang, S., S. Karato, J. Fitz Gerald, U. H. Faul, and Y. Zhou (2000), Simple shear deformation of olivine aggregates, *Tectonophysics*, *316*(1–2), 133–152, doi:10.1016/S0040-1951(99)00229-2.

Zhang, Y., B. Hobbs, and M. Jessell (1994), The effect of grain-boundary sliding on fabric development in polycrystalline aggregates, *J. Struct. Geol.*, *16*(9), 1315–1325.